AN ABSTRACT OF THE THESIS OF

Amadou Tidiane Camara for the degree of Master of Science in Chemical Engineering presented on December 5, 1997. Title: Modeling and Simulation of CF_4/O_2 Microwave Plasma Afterglows.

Abstract approved:

Redacted for Privacy

Milo Koretsky

A gas phase kinetic model for the CF_4/O_2 microwave discharge plasma and afterglow of our laboratory has been developed. A reaction pathway identifying the major chemical reactions is proposed. The rate coefficients of the electron impact dissociation reactions are determined at three different plasma powers using both published electron molecule collision cross section data and plug flow analysis of data collected in our system. Agreement between calculated and experimental rate coefficients is better than 20%. Fluid simulations of a two-dimensional mathematical model were performed using computational fluid dynamics. It is found that the model reproduced qualitatively the general trends of the experimental data. The effects of plasma power, feed gas composition, residence time and pressure on the product distribution of the system are studied. CF_4 conversion increases with power and residence time. The variation of CF_4 conversion and carbon containing species

distribution falls into two regimes. In the oxygen rich regime (below 25 mole % CF_4 in the feed), CO_2 is found to be the major product of CF_4 decomposition; homogeneous recombination reactions between atomic oxygen and the free radicals are found to be the dominant mechanism in the afterglow region resulting in high CF_4 conversions. Homogeneous reactions convert CO to CO_2. In the CF_4 rich regime (above 50 mole % CF_4), COF_2 is found to be the major product of CF_4 decomposition. Recombination reactions of CF_3 with atomic fluorine dominate in the afterglow region and limit conversion. Lowering pressures result in increased conversion of CF_4 and increased concentration of the carbon containing species.

MODELING AND SIMULATION OF CF_4/O_2 MICROWAVE PLASMA AFTERGLOWS

by

Amadou Tidiane Camara

A THESIS

submitted to

Oregon State University

in partial fulfillment of
the requirements for the
degree of

Master of Science

Completed December 5, 1997
Commencement June 1998

Master of Science thesis of Amadou Tidiane Camara presented on December 5, 1997

APPROVED:

Redacted for Privacy

Major Professor, representing Chemical Engineering

Redacted for Privacy

Head of Department, Chemical Engineering

Redacted for Privacy

Dean of Graduate School

I understand that my thesis will become part of the permanent collection of Oregon State University libraries. My signature below authorizes release of my thesis to any reader upon request.

Redacted for Privacy

Amadou Tidiane Camara, Author

TABLE OF CONTENTS

TABLE OF CONTENTS (CONTINUED)

LISTS OF FIGURES

LIST OF FIGURES (CONTINUED)

LIST OF FIGURES (CONTINUED)

LIST OF TABLES

LIST OF APPENDIX FIGURES

MODELING AND SIMULATION OF CF_4/O_2 MICROWAVE PLASMA AFTERGLOWS

CHAPTER 1

INTRODUCTION

The size of microelectronics devices is steadily decreasing; the smallest feature size, or critical dimension, has gone from 2 μm in 1980 to 0.25 μm in 1998. Along with the reduction of the device's critical dimension, the integrated circuit (IC) industry has introduced larger wafer sizes to increase the number of chips per wafer. Eight inch diameter wafers were widely used in the early 1990's but currently there is a strong drive towards the introduction of 12-inch diameter wafers. The challenges brought about by this transition are added to others created by the increased complexity and functionality of the IC. One such challenge will originate from plasma assisted etching. Plasma etching is used to remove many materials, including polymers such as photoresist and polymer containing dielectrics (IC delays are limited by the metallization scheme, low dielectric constant polymeric materials will need to be adopted). The necessity to accurately reproduce numerous mask patterns in the film of semiconductor devices has made plasma etching a critical step. These techniques permit the generation of anisotropic etch profiles with good selectivity and high etch rates (plasma etching allows the final etched feature to be within 10% of its dimension in the mask). With the introduction of the new processing equipment designed for 12-inch diameter wafers, the microelectronics industry will need to achieve better performance in the following areas: uniformity, etch rate,

selectivity to underlying material, and low etch-induced substrate damage. Surface damage occurs when the substrate is exposed to energetic particle and photon bombardment.

Plasma assisted downstream etching (PADE) techniques are used to minimize ion and radiation damage where etch anisotropy is not critical. For 0.18 μm critical feature dimension and less, PADE is currently the method of choice in the industry for the removal of residual polymeric materials. More recently, it is also being used in the manufacturing of multilayer printed circuits boards (PCB). After the mechanical drilling of through holes in the PCB, CF_4/O_2 microwave plasmas are used to remove the residual polymeric smear. Moreover, plasma etching provides a possible replacement to mechanical drilling of microvias (micro-sized holes that are less than 100 μm). These processes are mainly concerned with obtaining a high polymer etch rate.

The plasma environment is complex because it contains a large number of elementary processes occurring simultaneously (electron molecule collisions, radical chemistry, reactive species transport and surface recombination). Hence, developing optimum process conditions by trial and error can be expensive and time consuming. Computer simulations are a cheaper alternative that can provide valuable information on the plasma etching processes, which have mostly been developed empirically. In recent years, numerous studies (Smolinsky, 1979; Plumb, 1986; Jensen, 1990; Economou, 1991) have investigated the gas phase chemistry of CF_4/O_2 plasmas, which are currently widely used to remove silicon, silicon dioxide, photoresist and other polymeric films. Most of the studies have used the kinetic reaction scheme developed by Plumb and Ryan as the

basis of their simulations (Plumb, 1986). Although, the mechanism and rate constants of the gas free radical reactions are unaltered when used, there is little agreement on the values used for the rates of the electron impact dissociation reactions occurring in the glow discharge. Furthermore, most of these studies focused primarily on rf generated plasmas and relied on experimental data from other sources.

The goals of this research project are to:

1. Develop a gas phase kinetic model for the CF_4/O_2 microwave discharge plasma and afterglow of our laboratory by determining the rate coefficients of the electron impact dissociation reactions using both published electron molecule collision cross section data and plug flow analysis of data collected in our system.
2. Verify the adequacy of the kinetic model by performing computer simulations of a two-dimensional mathematical model using computational fluid dynamics.
3. Investigate the effect of operating parameters such as pressure, plasma power, gas flow rate and composition on the conversion and species distribution in the discharge.

A CF_4/O_2/Ar microwave discharge plasma is currently studied in our laboratory for the etching of polyphenylene oxide (PPO) epoxy samples. Preliminary experimental data shows that the maximum etch rate is obtained for a gas mixture composition of 20% CF_4/ 75% O_2/5% Ar. This study is intended to complement the experimental work.

There are six chapters in this thesis. Chapter 2 contains a literature review on the

relevant work about plasma chemistry and physics as well as the development of mathematical models. Chapter 3 presents a detailed description of the plasma model formulation. It includes the proposed kinetic model for the CF_4/O_2 microwave plasma of our laboratory and the determination of the rate coefficients of the electron impact dissociation reactions. The use of computational fluid dynamics to perform computer simulations of our kinetic model is described in Chapter 4. Chapter 5 presents and discusses the results of the computer simulations and compares them to experimental data collected in our laboratory. Finally, Chapter 6 summarizes the results of this work and recommendations for future work.

CHAPTER 2

LITERATURE REVIEW

2.1 Plasmas in Microelectronics

Plasma etching, which was first explored as a cheap and clean alternative to wet solvent resist stripping in the late 1960's, has become an indispensable tool in the fabrication of microelectronics devices. The first plasma reactors consisted of a vacuum system with parallel plate electrodes. When an electrical potential is applied to a gas flowing between the electrodes, a glow discharge plasma is formed. Reactive species which can chemically react with the substrate are created. The substrate is also directly exposed to energetic particle and photon bombardment; it can experience both shallow and deep surface damage when struck by particles or high energy radiation. The damage can alter the electrical characteristics of the device and degrade its performance. Because charged species are confined to the plasma region, placing the substrate outside of the discharge region can reduce the damage from ion bombardment. Plasma-assisted downstream etching (PADE) techniques are used to that effect in order to minimize the damage. During PADE, the active species are created in the discharge region before being transported by gas flow downstream in the etching chamber housing the substrate. Currently, PADE is widely used for the stripping of photoresist using CF_4/O_2 discharges.

2.2 Modeling of the Chemistry CF_4/O_2 Plasmas

Numerous publications have addressed the detailed chemical modeling of CF_4/O_2 discharge plasmas for the etching of silicon. Smolinsky and Flamm studied the stable products detected downstream of CF_4/O_2 plasma experimentally (Smolinsky, 1979). In their work, mixtures of CF_4/O_2 flowing in a 1.9 cm i.d. alumina tube were excited by a 49 W, 13.56 MHz discharge extending over approximately 5 cm of the tube length. Sampling of the effluent from the discharge was done by mass spectrometry with the inlet pinhole located 15 cm downstream from where the discharge commenced. Based on a series of kinetic studies, Plumb and Ryan developed an extensive kinetic model of CF_4/O_2 discharge plasma that proposed the major chemical species, the gas-phase reactions mechanisms and the rate of those reactions (Plumb, 1986). They then compared predicted concentrations to the experimental data of Smolinsky and Flamm. The proposed model consists of 12 species participating in 49 chemical reactions. Among those reactions, they identified a subset of 14 reactions that can describe adequately the gas phase chemistry (a more detailed description of the gas phase chemistry is presented in Chapter 3).

The main reaction products of a CF_4/O_2 discharge plasma are COF_2, CO_2, CO, O, F and F_2; the dependence of the concentrations of COF_2 and CO_2 on the mole percent of O_2 in the feed gas led Plumb and Ryan to identify COF as an important intermediate in the formation of these by-products (Plumb, 1984).

COF is produced by the reaction of CF_2 with oxygen atoms as:

$$CF_2 + O \rightarrow COF + F \qquad 2.1$$

In another study, it was shown experimentally that CF_2 is the main product of the electron-impact dissociation of CF_4 in the plasma (Plumb, 1986b). The following reactions were suggested as the major reaction pathways of COF in the plasma to the formation of COF_2 and CO_2 (Plumb, 1984):

$$COF + O \rightarrow CO_2 + F \qquad 2.2$$

$$COF + F \rightarrow COF_2 \qquad 2.3$$

At low mole percent of oxygen in the feed, the low concentration of O atoms in the plasma favors the reaction of COF with atomic fluorine to produce COF_2, which then becomes the dominant stable product in the effluent gas. In an oxygen rich environment, the reaction of COF with atomic oxygen to produce CO_2 becomes the major reaction.

The rate mechanisms and constants of the set of gas phase free radical reactions are widely used in various studies of the modeling of CF_4/O_2 plasma found in the literature (Economou, 1989; Baltes, 1989; Venkatesan, 1990; Jensen, 1990), but the rate constants of the electron impact dissociation reactions were identified as "the uncertain aspect of their model" (Plumb, 1986). The difficulty in determining the electron impact rate constants stems from the fact they are dependent on factors such as the electron density and the electron energy distribution in the plasma. Those factors are very difficult to measure experimentally and numerous simplifying assumptions have to be made in order to determine them. Plumb and Ryan performed a plug flow analysis of the experimental downstream mass spectrometric data of the alumina discharge transport tube provided in the literature (Smolinsky, 1979) in order to determine those rate constants for their study (Plumb, 1986). Such an approach makes the implicit assumption

that the electron density and the electron energy distribution are uniform throughout the plasma region. Thus, the low level of information available in the literature on the electron density and the electron energy distribution makes the rate constants of the electron impact reactions difficult to determine. The studies that base their gas phase model on the proposed kinetic model (Plumb, 1986) attempt to account for that uncertainty. In a similar study, Jensen and Dalvie used the rate coefficients as fitting parameters to adjust for the difference in geometry existing between their system and that of Plumb and Ryan (Jensen, 1990).

Economou and Park, and Bates et al. have assumed the rate coefficients to be linearly dependent on the electron density (Economou, 1991; Bates, 1989). Based on the reactor parameters provided by Plumb and Ryan, they have calculated the electron density and derived a general expression for the rate constants (Plumb, 1986). The lack of reliable electron impact dissociation rate constant for the CF_4/O_2 microwave discharge plasma in the literature has motivated this study. Subsequently, there is an attempt to determine these rate coefficients by considering both the physical and chemical characteristics of our PADE system.

2.3 Modeling of Plasma Physics

The complex nature of the plasma environment couples both plasma physics and plasma chemistry and forces most studies to focus on only one of these elements. Plasma physics deals with the electrical characteristics of the plasma which includes the density of the charged particles, the strength of the electric field and the electron energy

distribution. It influences directly plasma chemistry since most chemical reactions in a CF_4/O_2 discharge are initiated by electron molecule collisions and their importance depend on the kinetic energy of the plasma electrons. The direct measurement of the electrical characteristics of the plasma is difficult but several examples can found in the literature. Chou and Phillips have measured both the electron energy distribution function and the average electron energy of a 250 W oxygen and argon microwave discharge plasma (Chou, 1992). The experimental method used, the modified langmuir probe technique developed by Druyvesteyn, consists in introducing a 0.5 mm diameter tungsten wire inside a plasma and applying a known potential to the probe. The electron current drawn by the probe is then measured and leads to a Langmuir I-V characteristic curve from which both the electron energy distribution function (EEDF) and the average electron temperature can be derived. The authors have also reported measured trends in temperature as a function of distance from the plasma. Similarly, Moisan et al. have experimentally determined the EEDF, the average electron temperature and the electron density of a rf O_2 plasma (Moisan, 1987). The experimental data obtained by these studies does not to account for the effect of the probe on the plasma. The introduction of the probe in the plasma can alter its electron energy distribution as well as the average electron energy.

Other studies (Mantzaris, 1995) have attempted to calculate the electron energy distribution function by solving the electron velocity distribution, which is defined as the density of electrons in phase space (both position and velocity space). A microscopic electron balance leads to the Boltzman equation from which the electron energy

distribution can be estimated. Mantzaris et al. have calculated the electron energy distribution of their system using a general Boltzman equation solver. Their program uses detailed electron molecule cross section data as its main input parameter and outputs parameters such as the electron energy distribution function and the electron density of the discharge (Mantzaris, 1995). In general such electron-molecule cross-section data can be found in the literature (Myers, 1968; Winters, 1986; Itikawa, 1989a; Tarnovsky, 1993); Christophorou et al., and Itikawa et al. have published a compilation of collision cross-section data of CF_4 and O_2, respectively, available in the literature (Christophorou, 1996; Itikawa, 1989b). The published experimental data carries a significant amount of uncertainty since the complex nature of the plasma environment makes the experimental determination of the collision cross-sections difficult. The accuracy of electron-molecules collision cross-sections is discussed in Chapter 3.

The above studies consider separately plasma physics and plasma chemistry. Although they provide valuable information on both areas, they do not consider systematically their coupled effects. For example, electrons collide mainly with the neutral gas, therefore the nature of the gas (its electron attachment cross-section) affects the discharge physical properties by its tendency to produce negative ions and change the electron energy balance. Conversely, the discharge physics influences its gas phase chemistry since many of the chemical reactions of a plasma are initiated by electron impact dissociation reactions.

In the present study, an attempt is made to take into consideration the physical properties of the CF_4/O_2 discharge plasma in developing a gas phase kinetic model. The

rate coefficients of the electron-impact dissociation reactions are determined both using published electron-molecule cross-section data and a plug flow analysis of data of our laboratory. The effect of parameters such as pressure, power, gas flow rate and composition on the discharge, are then examined. The kinetic model is used to perform fluid simulations of the plasma and the afterglow.

CHAPTER 3

PLASMA MODEL DEVELOPMENT

3.1 Glow Discharge Plasmas

A glow discharge plasma is a partially ionized gas with approximately equal numbers of positively and negatively charged species (electrons and ions) which can be generated by applying an electric potential to a volume of gas at a pressure in a range between 1 mtorr and 10 torr. The extent of ionization is typically small for these plasmas. Usually there is only one charged particle per 10,000 to 1,000,000 neutral atoms and molecules. In the bulk of the plasma, the electron density is normally in the range of 10^9 to 10^{12} cm^{-3}. Because their mass is a lot smaller than the ions, electrons receive most of the electrical energy applied to the plasma and are also highly mobile. The transfer of energy from the electrons in the discharge to the other species (neutrals and ions) is done through inelastic collisions and leads to the formation of new active chemical species (ions, free radicals, excited species, etc.). Typically, microwave (2.45 GHz) or radio frequency (13.56 MHz) sources generate the electrical energy which is applied. Microwave plasmas tend to have a higher electron density.

The distribution of products which results from the electron-molecule collisions is determined by the physical properties of the glow discharge such as the electron energy distribution function (EEDF), the electron density and the nature of the electric field. Unstable species are formed by electron-impact collisions and are continuously lost by homogeneous reactions and wall recombination. The balance between the formation and the loss of those species determines the steady concentration of each species in the

discharge. In this chapter, a model of the chemistry for a CF_4/ O_2 downstream microwave plasma is developed.

3.2 Microwave Plasma Set-up

Figure 3.1 shows the schematic of the downstream microwave etch system in our laboratory that is modeled. It consists of a microwave plasma, a reaction chamber, a mass spectrometer and an optical emission spectrometer. The microwave plasma creates active chemical species that are then transported downstream by gas flow in the reaction chamber where the substrate is located. The mass spectrometer is situated in the reaction chamber where it analyzes the composition of the downstream effluent gas.

The gas mixture of CF_4, O_2 and Ar is introduced and carried through the microwave discharge plasma by a quartz tube of 1.86-cm I.D. and 50.80 cm total length. The plasma cavity extends over 5 cm of the tube and its electrical energy is supplied by a microwave power generator operating at 2.45 GHz with a power ranging from 50 to 1000 W. The gas transport tube which carries the plasma species is inserted horizontally 5 cm into the reaction chamber. The substrate holder, located 3-cm downstream of the end of the quartz tube in the reaction chamber, is mounted normal to the gas transport tube.

The sampling cone of the mass spectrometer is located right behind the substrate holder; it leads to a chamber where low pressure creates a molecular beam of the sampled gas which is then introduced in the analytical chamber through a skimmer cone. The spectrometer is linked to a computer, which collects the raw mass intensities, which identifies the different gaseous species.

A detailed explanation of the collection and analysis of the mass spectrometric data is given elsewhere (Hsu, 1997).

Figure 3.2 shows the geometry of the axisymmetric microwave plasma modeled in this chapter. Fluid simulations of active species (Chapter 5) are done both in this simpler geometry, and with a more complicated geometry (not presented), which includes the substrate, shown in Figure 3.1. The reactant gases include CF_4, O_2 and Ar. The exit of the tube contains, in addition to the reactants, stable products (CO_2, CO, COF_2 and F_2) and long lived free radicals (O and F). Most reactive free radicals produced in the plasma such as CF_2 and CF_3, react completely. Similarly, no charged species (ions or electrons) are present at the exit downstream of the plasma.

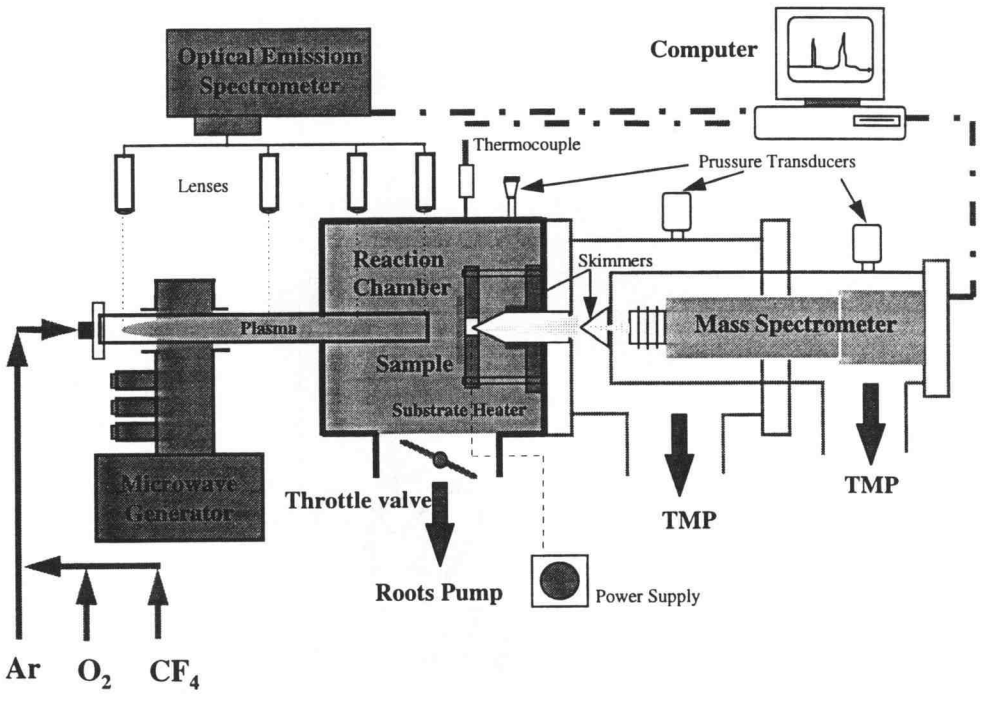

Figure 3.1: The schematic diagram of experimental downstream microwave plasma system

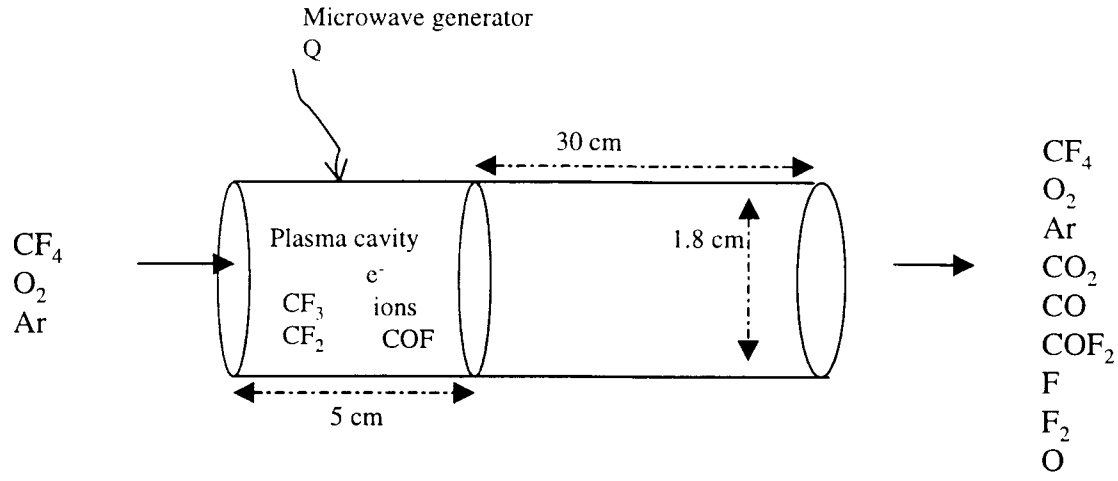

Figure 3.2: Schematic of the geometry used in the plasma model of the CF_4/O_2 microwave discharge.

3.3 Selection of a reaction pathway

There are many possible reactions in a CF_4/ O_2 plasma. Therefore, in modeling a discharge plasma, it is essential to identify the reacting species as well as the rates and mechanisms of the reactions between them. Plumb and Ryan have proposed an extensive kinetic model of CF_4/O_2 discharge plasma that consists of 22 chemical species participating in 49 reactions (Plumb, 1986). The authors have developed the chemistry model by experimentally measuring the rate coefficients of several gas phase free radical reactions. Based on these studies, a reduced set of reactions is considered. The reaction pathway for the CF_4/O_2 microwave discharge used in this thesis is shown in Figure 3.3 and summarized in Table 3.1. It describes the major chemical species present in the system as well as the path to the formation of the major stable products.

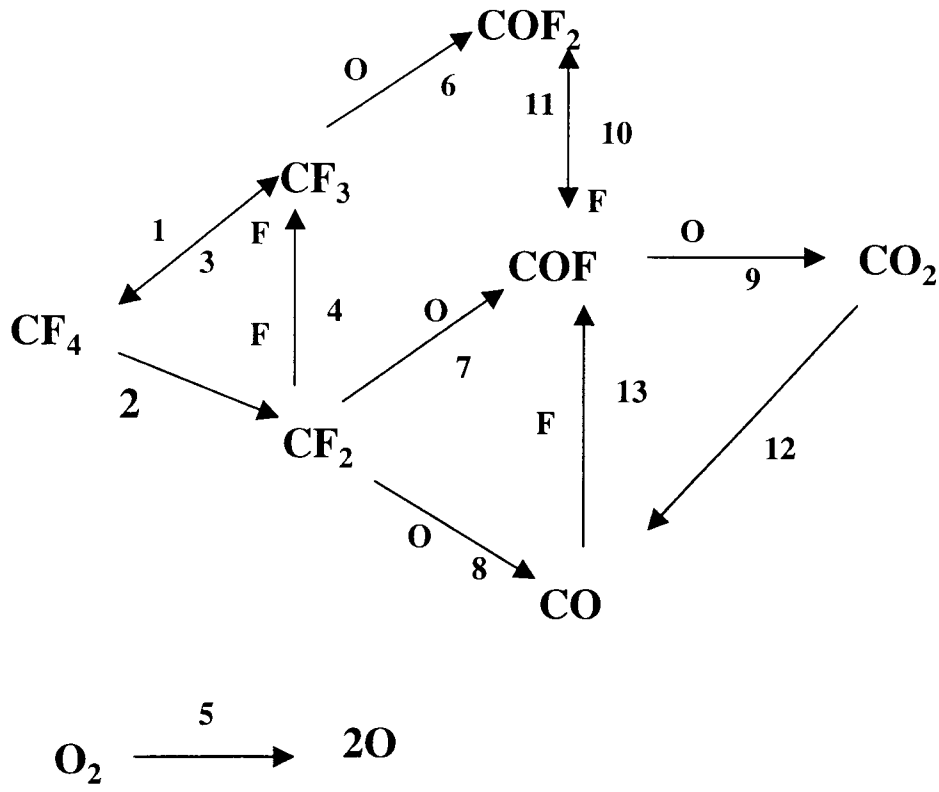

Figure 3.3: Major Reactions in the CF_4/ O_2 Plasma

Table 3.1: Rate constants of the recombination reactions used in the simulation (Plumb, 1986).

Reaction Number	Reaction	Rate Coefficient
1	$CF_3 + O \rightarrow COF_2 + F$	3.11×10^{-11}
2	$CF_2 + O \rightarrow COF + F$	1.4×10^{-11}
3	$CF_2 + O \rightarrow CO + 2F$	4×10^{-12}
4	$COF + O \rightarrow CO_2 + F$	9.3×10^{-11}
5	$COF + F \rightarrow COF_2$	8×10^{-13}
6	$CO + F \rightarrow COF$	1.3×10^{-15}
7	$O_2 + F \rightarrow FO_2$	1.8×10^{-16}
8	$FO_2 + F \rightarrow F_2 + O_2$	5×10^{-11}
9	$FO_2 + O \rightarrow F + O_2$	5×10^{-11}
10	$CF_2 + F \rightarrow CF_3$	4.2×10^{-13}
11	$CF_3 + F \rightarrow CF_4$	1.3×10^{-11}
12	$2CF_3 \rightarrow C_2F_6$	8×10^{-12}
13	$O(1D) \xrightarrow{wall} O$	2×10^{3}

Units of s^{-1} (for first order reaction) or $cm^3 s^{-1}$ (for second order reaction).

According to the above model, CO_2, CO and COF_2 are the main stable products of the decomposition of CF_4 in the CF_4/ O_2 discharge plasma. COF_2 arises mainly from the reaction of CF_3 and atomic oxygen while CO and CO_2 are derived from CF_2.

3.4 Determination of the Recombination and Dissociation Reactions Rate Constants

3.4.1 Determination of the Dissociation Reactions Rate Constants:

Consider a generic electron impact inelastic collision. The chemical reaction can be describe as follows:

$$e + M \rightarrow P_1 + P_2 + e \qquad 3.1$$

where M is the reactant molecule and P_1 and P_2 are reaction products. These products may be reactive neutral fragments in the case of electron impact dissociation or an ion and an electron for electron impact ionization. The reaction rate, *R*, for the process described by Equation 3.1 is given by:

$$R = k_i \cdot n_e \cdot n_M \qquad 3.2$$

where k_i is the second order rate constant, n_e is the electron density in the plasma and n_M is the density of the reactant molecule M. Electron impact reactions can also be written in pseudo-first order form:

$$R = k_i' n_M \qquad 3.3$$

where $k_i' = k_i n_e$

The dissociation reactions that occur to in a CF_4/O_2 discharge plasma include:

$$e + CF_4 \rightarrow CF_3 + F + e \quad 3.4$$

$$e + CF_4 \rightarrow CF_2 + 2F + e \quad 3.5$$

$$e + O_2 \rightarrow 2O + e \quad 3.6$$

$$e + CF_4 \rightarrow CF_3^+ + F + 2e \quad 3.7$$

The electron impact dissociation rates constants can be derived from kinetic theory:

$$k_i \left(cm^3/s\right) = \int_0^\infty \sqrt{\left(\frac{\varepsilon}{2m}\right)} \sigma_i(\varepsilon) f(\varepsilon) d\varepsilon \quad 3.8$$

where ε is the electron energy, σ_i is the collision cross-section for process (i), and $f(\varepsilon)$ is the electron energy distribution function (EEDF). In order to use the above expression to calculate the electron-impact dissociation rates, one needs to estimate the electron impact dissociation cross-sections of the species involved.

The molecular collision cross-sections are obtained from the literature for CF_4 and O_2. For CF_4, the total dissociation cross section ($\sigma_{diss,t}(\varepsilon)$), the dissociation cross section into the neutrals CF_2 and CF_3 ($\sigma_{diss,neut,t}(\varepsilon)$) as shown by Equations 3.4 and 3.5 and the ionization cross section ($\sigma_{i,t}(\varepsilon)$) illustrated by Equation 3.7 are available in the literature [(Winters, 1982), (Sugai, 1995) and (Christophorou, 1996) respectively]. Figure 3.4 shows a plot of $\sigma_{diss,t}(\varepsilon)$ (Winters, 1982), $\sigma_{i,t}(\varepsilon)$ (Christophorou, 1996) and $\sigma_{diss,neut,t}(\varepsilon)$ (Sugai, 1995) as a function of electron energy.

The direct measurement of the total dissociation cross section into neutrals is difficult because of the current experimental limitations associated with the detection of low energy neutrals. Up to date, only one such data set has been reported (Sugai, 1995). Other available measurements have attempted to indirectly determine the total neutral

dissociation cross section by subtracting $\sigma_{i,t}(\varepsilon)$ from $\sigma_{diss,t}(\varepsilon)$ (Bonham, 1994). The threshold energy for CF_4 dissociation was estimated to be near 12.5 eV which is lower than its ionization potential (16.2 eV) (Winters, 1982). Therefore, at low electron impact energies (near threshold), the neutral dissociation of CF_4 dominates while the dissociative ionization process (production of ions and neutral species) becomes progressively dominant at energies above 16.2 eV. Below 30 eV, the magnitude of $\sigma_{diss,t}(\varepsilon)$ is much greater than $\sigma_{i,t}(\varepsilon)$ and the indirect measurement method used to determine $\sigma_{diss,neut,t}(\varepsilon)$ should be valid (Bonham, 1994). However, these data are greater by almost two orders of magnitude than the values directly measured (Sugai, 1995).

For our calculations, the total dissociation cross sections for CF_4 measured by Winters and Inokuti was used (Winters, 1982). These values have a reported uncertainty of ±20%. The selection of $\sigma_{diss,t}(\varepsilon)$ over $\sigma_{diss,neut,t}(\varepsilon)$ is reasonable because dissociative ionization is negligible near the threshold dissociation energies where the neutral dissociation of CF_4 is dominant and $\sigma_{diss,neut,t}(\varepsilon) \approx \sigma_{diss,t}(\varepsilon) - \sigma_{i,t}(\varepsilon)$.

For O_2, the situation is less satisfactory since no reliable data is available for the total dissociation cross-section. The oxygen molecule easily dissociates and perturbations among its electronically excited states make its experimental study difficult. Itikawa et al. published an extensive literature review on the collision processes involving oxygen molecules and electrons and also outlined the uncertainty involved in the existing experimental data (Itikawa, 1989). Differences of up to 2 orders of magnitude exist between the literature oxygen cross-section data.

Therefore, in the present study, the rate of oxygen dissociation by electron collisions was not calculated but rather inferred from experimental measurements.

For a rigorous calculation of the rate constant k_i, the exact form of the EEDF for our microwave system needs to be determined. The EEDF is usually derived from the electron velocity distribution function and directly related to the nature of the electron-molecule collisions; in the plasma, these interactions occur through elastic and inelastic collisions.

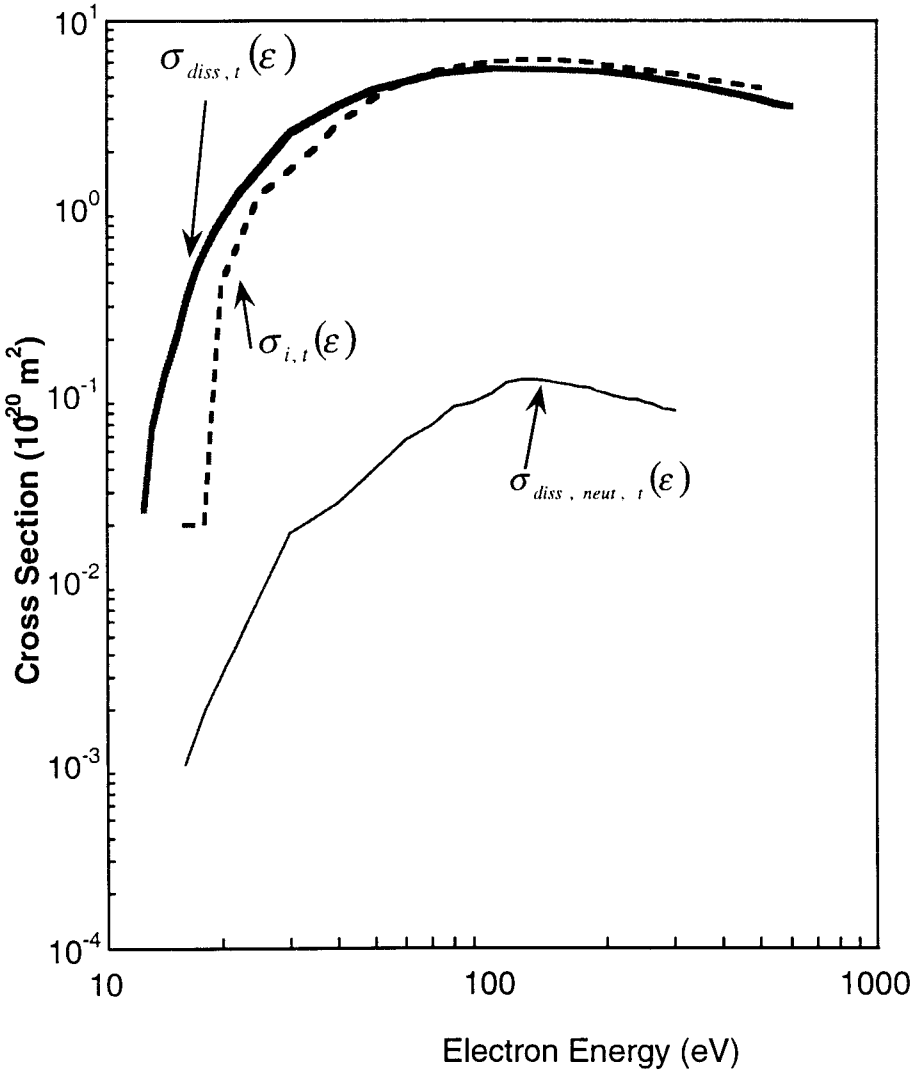

Figure 3.4: Comparison of $\sigma_{diss,t}(\varepsilon)$ (Winters, 1982), $\sigma_{i,t}(\varepsilon)$ (Christophorou, 1996) and $\sigma_{diss,neut,t}(\varepsilon)$ (Sugai, 1995).

The transfer of energy is inefficient during elastic collisions since the particles exchange momentum and kinetic energy without affecting their internal states. The creation of active species occurs through inelastic collisions when the average electron energy is high enough to cause electronic transitions between energy states. Thus, the higher the number of high-energy electrons the EEDF predicts, the more efficient the discharge will be in creating active species.

The EEDF is very difficult to determine. A microscopic electron balance must be solved in phase (r, v) space. The resulting equation is known as the Boltzmann equation. In order to rigorously solve the Boltzmann equation, all collisions that the electrons undergo must be quantified. In practice, several simplifying assumptions are often made. If the frequency of the applied field is less than the characteristic collision frequency and the momentum collision cross-section varies as $(1/v)$, a Maxwellian energy distribution function results:

$$f(\varepsilon) = 2.07 \cdot \langle \varepsilon \rangle^{-3/2} \cdot \varepsilon^{1/2} \cdot e^{\frac{-1.5\varepsilon}{\langle \varepsilon \rangle}} \qquad 3.9$$

where $\langle \varepsilon \rangle$ is the mean electron energy. When the momentum collision cross-section is independent of the electron velocity, a Druyvestein energy distribution function results:

$$f(\varepsilon) = 1.034 \cdot \langle \varepsilon \rangle^{-3/2} \cdot \varepsilon^{1/2} \cdot e^{\frac{-.545\varepsilon^2}{\langle \varepsilon \rangle^2}} \qquad 3.10$$

In the absence of the solution to the Boltzmann equation, Plumb and Ryan approximated the distribution in their system to be close to Druyvestein with mean electron energy of 5.9 eV. Figure 3.5 shows a comparison of Maxwellian and Druyvestein distribution functions for a mean electron energy of 5.9 eV.

The Druyvestein distribution predicts fewer higher energy electrons than does the Maxwellian distribution. Since most inelastic processes require high energy, less reactive species are created.

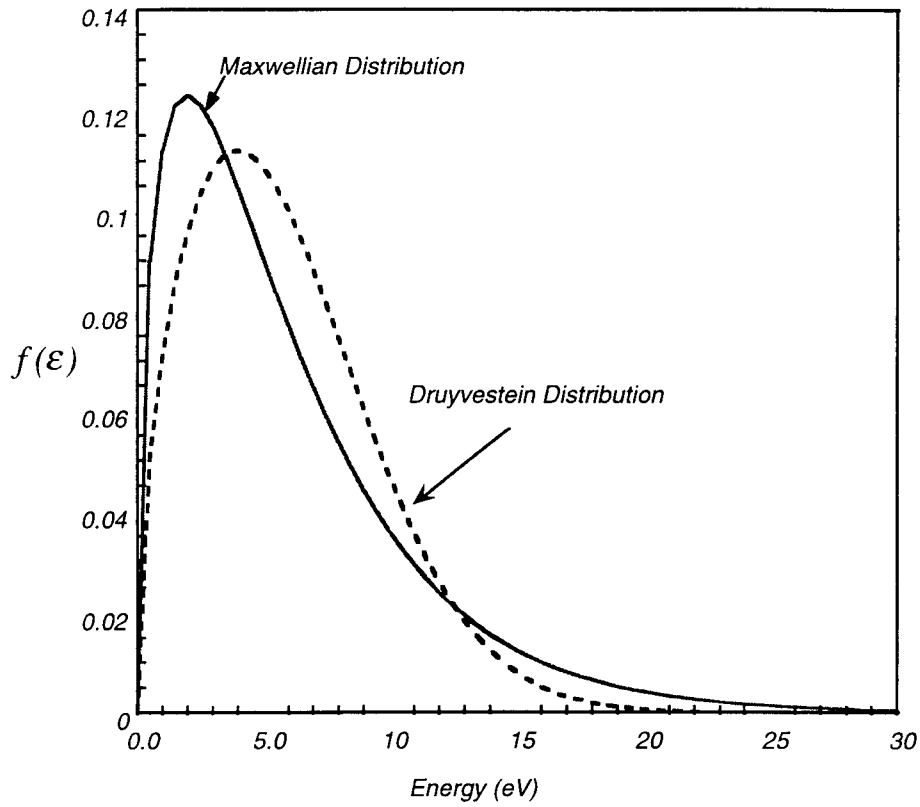

Figure 3.5: Maxwellian and Druyvesteyn energy distributions, both with average energy of 5.9 eV.

The pseudo first order dissociation rate constants for CF_4 at 0.5 torr are calculated using Equation 3.8 and assuming that the EEDF is Druyvestein with mean electron energy 5.9 eV. The cross-section data reported by Winters and Inokuti and shown in Figure 3.4 was fit to a sixth order polynomial function. The resulting rate coefficient was

converted to a pseudo-first order rate constant by multiplying the result obtained by integration and the average electron density shown in Table 3.2.

The electron density in the plasma is related to power by:

$$P = n_e e \mu_e E_{rms}^2 \qquad 3.11$$

where P is the power density (W/cm^{-3}), n_e is the electron density, e is the electronic charge and μ_e is the electron mobility at the mean root square electric field E_{rms}. At 0.5 torr, Plumb and Ryan have postulated that $E_{rms} = 22.5$ v cm^{-1} and $\mu_e = 7\times10^5$ $cm^2v^{-1}s^{-1}$ for their system (Plumb, 1986). The variation of the electron density with power is shown in Table 3.2. Table 3.3 shows the calculated electron impact dissociation rate constants for different plasma power.

Table 3.2: Variation of electron density with power

Power (W)	Plasma Density (cm^{-3})
50	6.9×10^{10}
100	1.38×10^{11}
150	2.08×10^{11}

Table 3.3: Calculated electron dissociation rate constants in units of s^{-1} for different plasma power at 0.5 torr

Reaction	P = 50 W	P = 100 W	P = 150 W
$CF_4 + e \rightarrow CF_3 + F + e$ $\rightarrow CF_2 + 2F + e$	25.87	52.12	78.00

The rate constants for the electron impact dissociation reactions were also obtained from experimental data from our plasma system. It consists of treating the electrical discharge as a plug flow chemical reactor, assumes a uniform electron density in the plasma region and treats the dissociation processes as pseudo-first order chemical reactions. Since the microwave plasma has no internal electrodes with large sheath fields, these assumptions are reasonable.

In a plug flow reactor the composition of the fluid varies from point to point along a flow path; consequently, the material balance for a reaction component must be made for a differential element of volume *dV*. Integration of the expression for the whole reactor gives the following equation.

$$\tau = C_{CF_{4,0}} \int_{0}^{x_{CF4,f}} \frac{dx_{CF_4}}{-r_{CF_4}} \qquad 3.12$$

where τ is the nominal discharge residence time in units of s^{-1} and $C_{CF_{4,0}}$ represents the feed concentration in CF_4. For a pseudo-first order reaction, the residence time is correlated to the conversion by the integrated expression of Equation 3.12:

$$k\tau = \ln\left(\frac{1}{1 - x_{CF_4}}\right) \qquad 3.13$$

where the conversion is defined as:

$$x_{CF_4} = \frac{F_{CF_4} - F_{CF_{4,0}}}{F_{CF_{4,0}}} \qquad 3.14$$

where $F_{CF_{4,0}}$ *and* F_{CF_4} are the inlet and outlet molar flow rates of CF_4, respectively.

A gas mixture of CF_4, O_2 and Ar was used. Argon is an inert gas and does not participate in any chemical reaction, therefore the conversion of CF_4 can be related to the change in the mole fraction of Argon during the process and Equation 3.14 becomes:

$$x_{CF_4} = 1 - \left(\frac{y_{Ar,i}}{y_{Ar,f}} \right) \left(\frac{y_{CF_4,f}}{y_{CF_4,i}} \right) \qquad 3.15$$

Equation 3.13 suggests that the rate coefficient for CF_4 dissociation can be determined by plotting the right hand side expression versus the residence time. The overall rate constant for the electron impact dissociation of CF_4 can be determined through a judicious choice of experimental conditions. The reaction pathway, shown in Figure 3.3, implies that in an oxygen dominated environment (mixture where the concentration of CF_4 is less than, for example, 20%), the reactions between oxygen and CF_4 dissociation products (CF_3+CF_2) dominate while the reactions between CF_3 or CF_2 and F to reform CF_4 are negligible. Therefore, the reduction in CF_4 mole fraction can be related to the overall CF_4 dissociation rate. A set of experimental runs are performed using a strategy where the feed composition in O_2, CF_4 and Ar are kept constant at 80, 15 and 5 percents respectively while the nominal residence time was changed (the overall volumetric flow rate was varied from 20 to 100 sccm). The experimental data consisted of the mass spectrometric analysis of the effluent downstream gas. Figures 3.6, 3.7 and 3.8 shows the plot of $\ln\left(\frac{1}{1-x_{CF_4}}\right)$ vs. τ (s^{-1}) for different experimental conditions. The determined rate constants are displayed in Table 3.4.

Likewise an estimate of the dissociation rate coefficient for O_2 can be made using a similar scheme. In a CF_4 dominated environment, the concentrations of O atoms is kept

low by reactions with radicals derived from CF_4 making the recombination reactions to reform O_2 downstream negligible. It should be noted that all these radical recombination reactions are exothermic and require a third body to conserve both energy and momentum. Figure 3.9 shows the plot of $\ln\left(\frac{1}{1-x_{CF_4}}\right)$ vs. τ (s^{-1}) for O_2 and 100 W plasma power. Table 3.4 summarizes the determined pseudo-first order rate constants for O_2.

Table 3.4: Determined electron dissociation rate constants in units of s^{-1} for different plasma power at 0.5 torr.

Reaction	P = 50 W	P = 100 W	P = 150 W
$CF_4 + e \rightarrow CF_3 + F + e$ $\rightarrow CF_2 + 2F + e$	18.2 ± 2.1	71.3 ± 2.9	154.7 ± 7.6
$O_2 + e \rightarrow O + O(1D) + e$ $\rightarrow 2O + e$		43.1 ± 5.08	

The estimated dissociation rate constants based on the percent conversion data of our laboratory are in good agreement with the calculated rate constants based on Equation 3.8. Table 3.5 compares calculated and experimental rate coefficients. The agreement is as good as can be expected, based on the assumptions of the model.

Table 3.5: Comparison between calculated and determined CF_4 dissociation rate constants at different power.

Power (W)	K_{exp} (s^{-1})	K_{calc} (s^{-1})
50	18.20	25.87
100	71.30	52.12
150	154.70	78.00

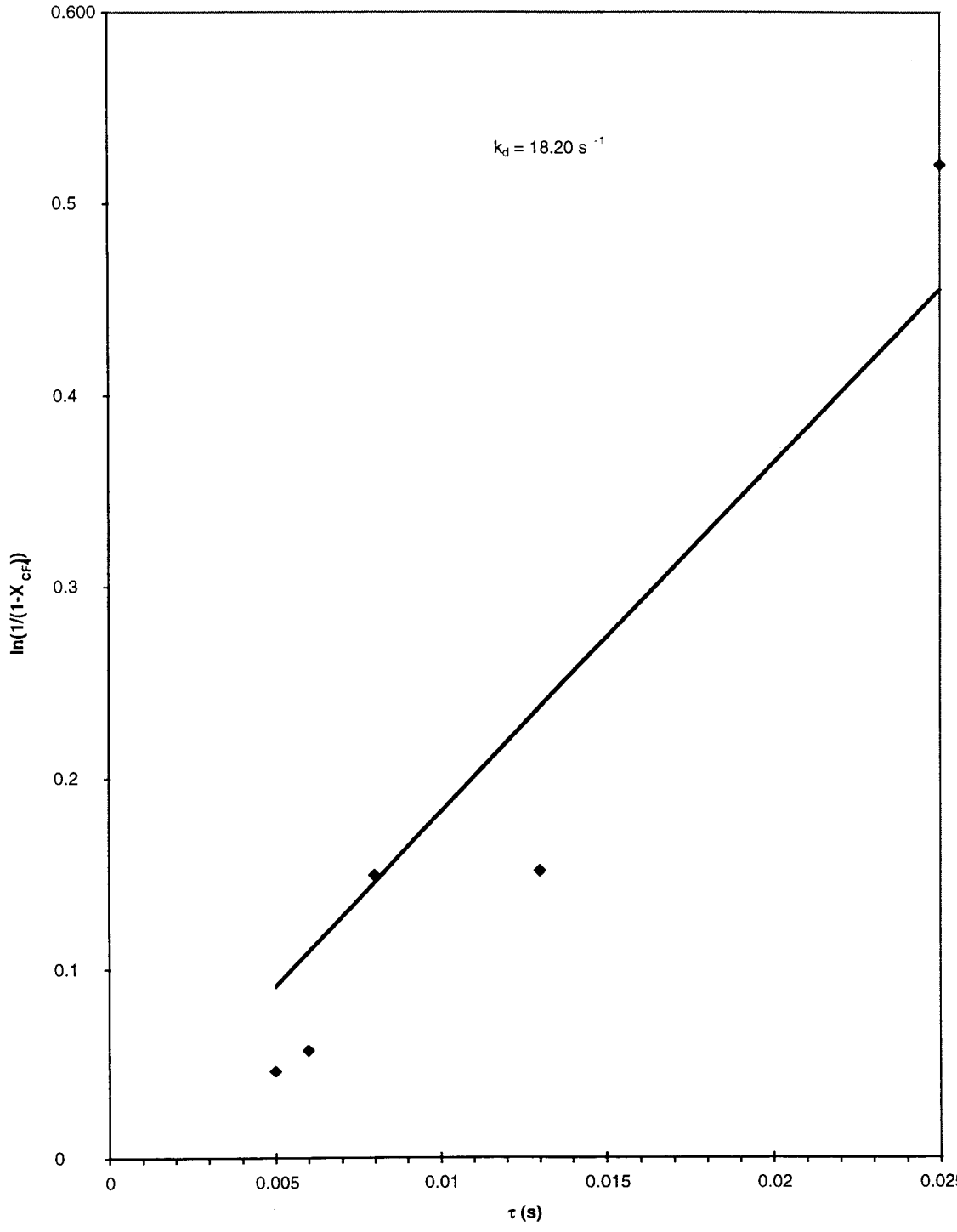

Figure 3.6: Determination of CF_4 pseudo-first order electron dissociation coefficient at 50 W.

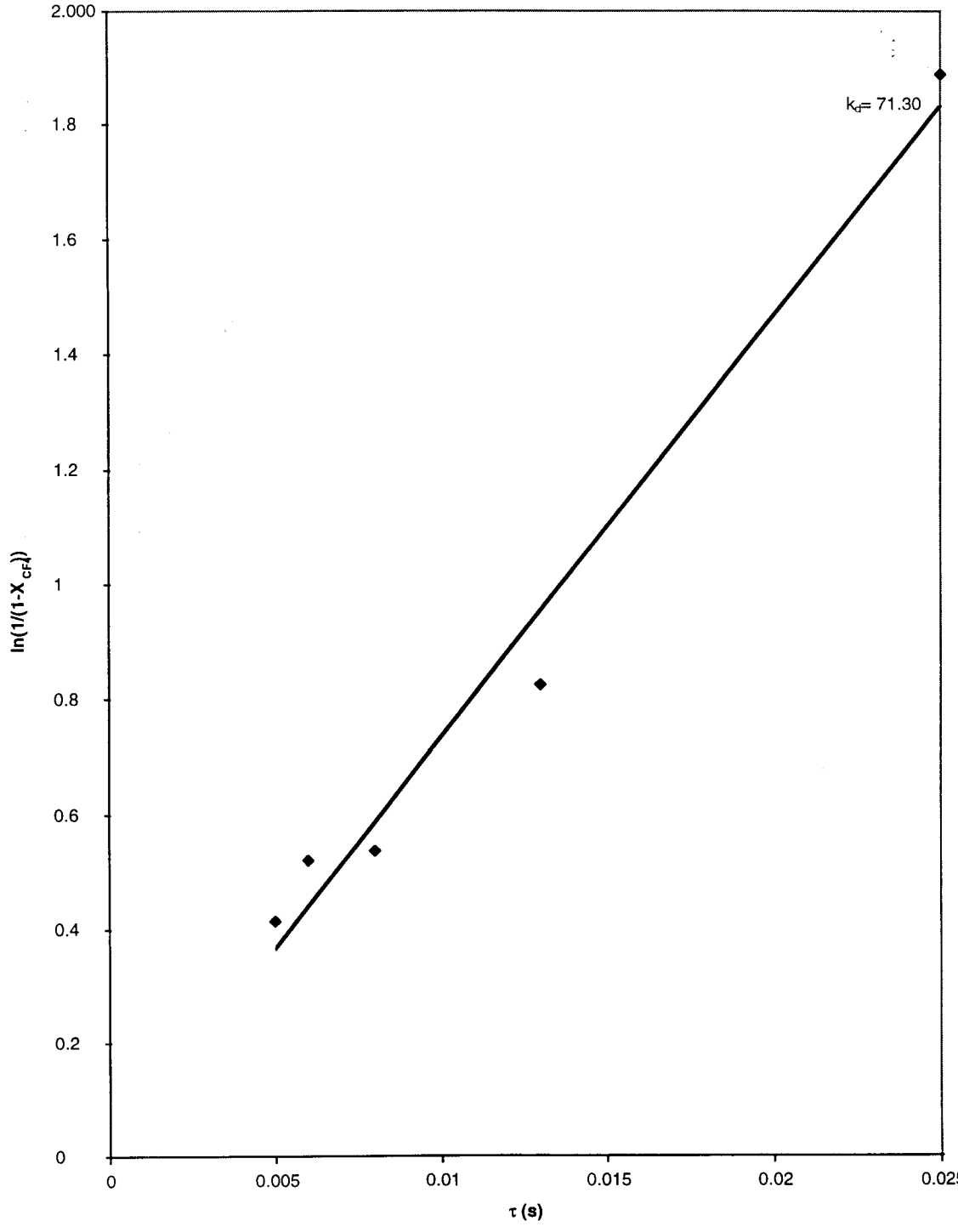

Figure 3.7: Determination of CF_4 pseudo-first order electron dissociation coefficient at 100 W.

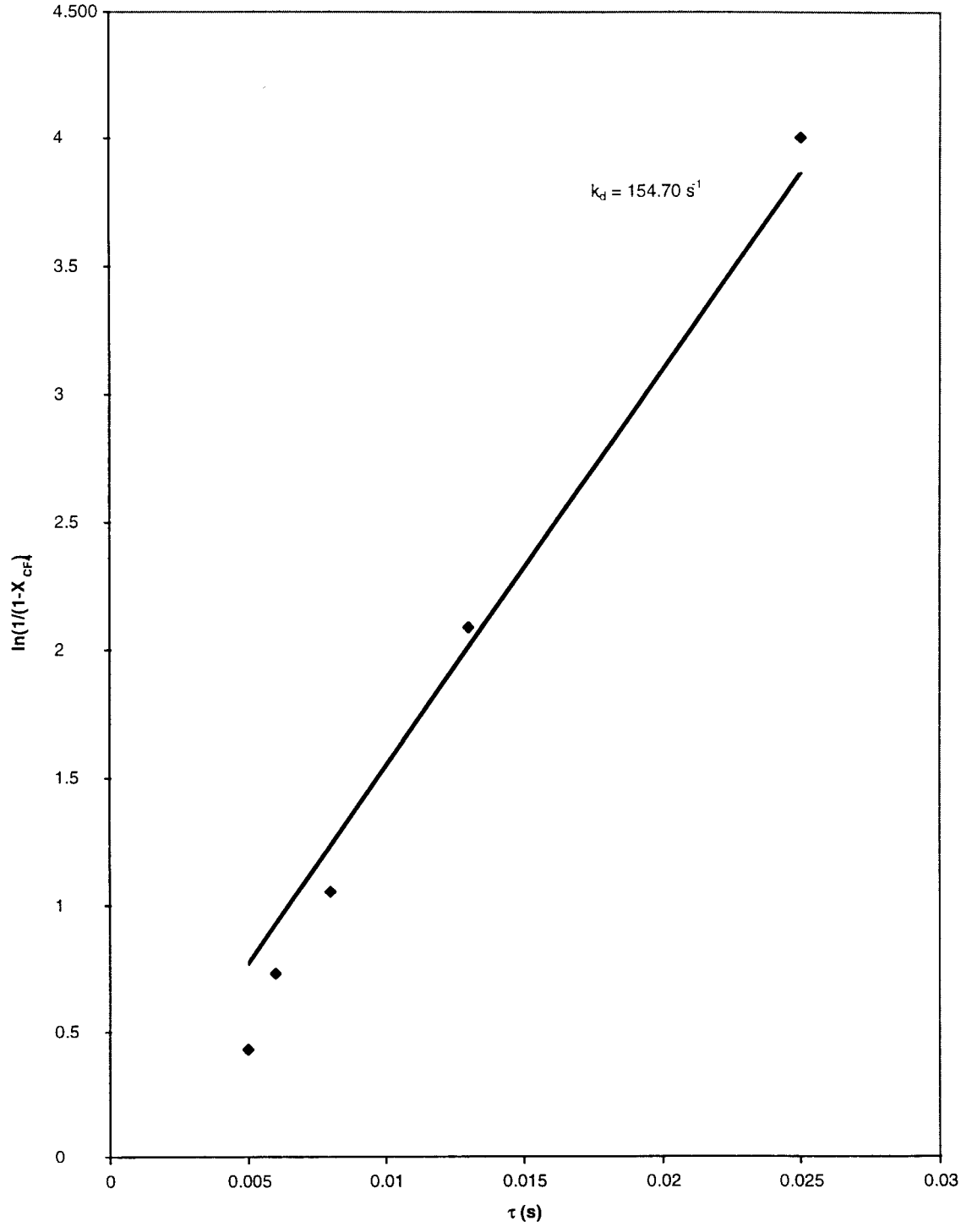

Figure 3.8: Determination of CF_4 pseudo-first order electron dissociation coefficient at 150 W

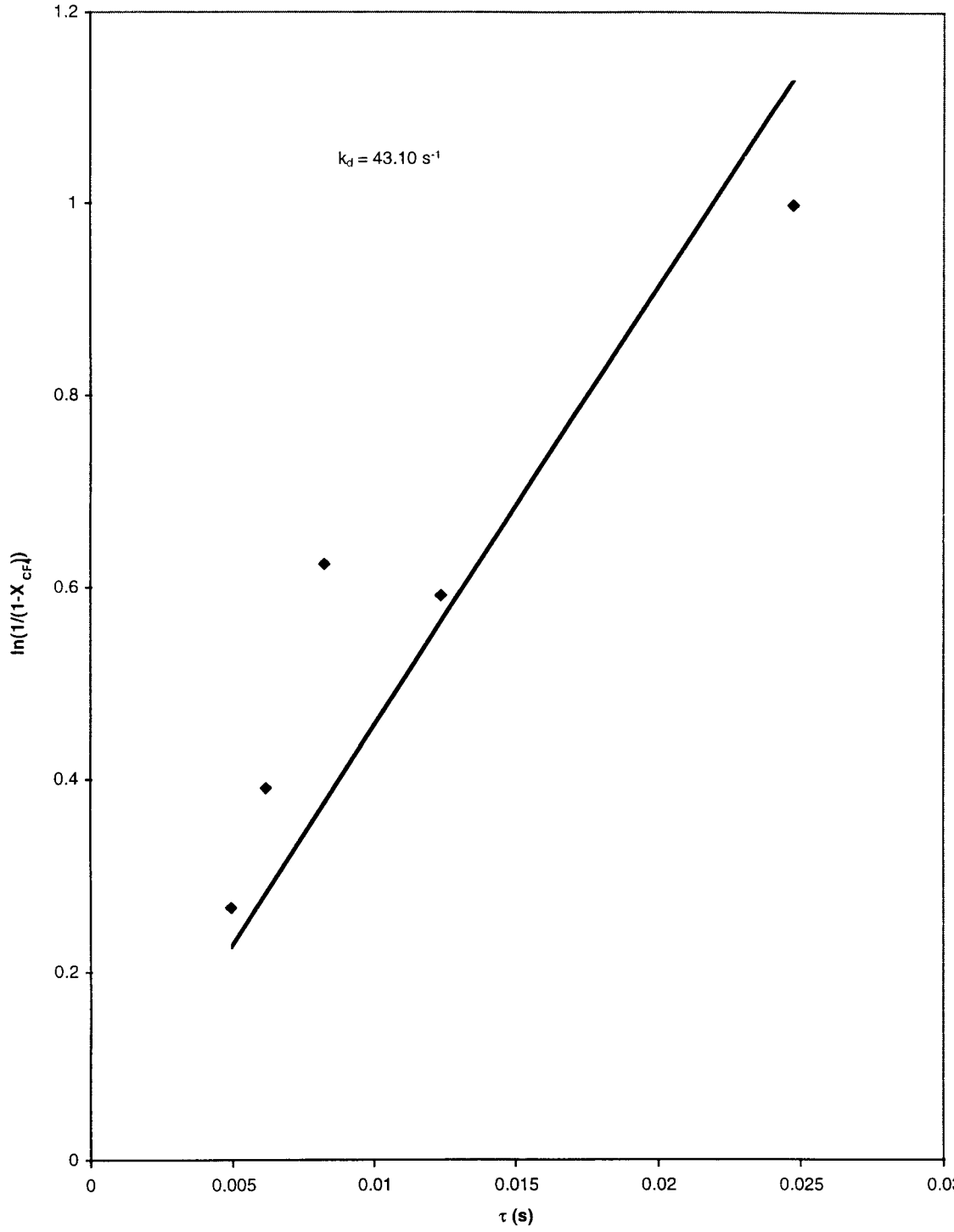

Figure 3.9: Determination of O_2 pseudo-first order electron dissociation coefficient at

A plot of k_d vs. power is shown in Figure 3.10. These data show that the experimental rate constant is a quadratic function of power while theory predicts that it should be linear. The experimental data suggest that a linear increase of the power results in the pseudo first order rate constant being increased as the power squared. One would expect from theory that the electron density n_e is linear with power density, while the electron temperature is independent of power density at a given pressure. A possible explanation may be that a linear increase in power leads to a linear increase in the rate constants and a linear increase in the discharge volume.

The branching ratio for CF_4 electron dissociation into CF_3 and CF_2 also needs to be quantified. An appropriate estimate of that ratio may be obtained by looking at the ratio of the number of moles of ($CO+CO_2$) formed during the reaction to that of COF_2, assuming that COF_2 is a direct product of CF_3 decomposition while CO and CO_2 come from CF_2.

The absence of adequate quantitative information did not allow the use of such an approximation. Instead, the branching ratio obtained by Plumb and Ryan is used (Plumb, 1986). From their experimental work, a ratio of the primary dissociation rate for CF_2 production to that of CF_3 is found to be 2.4 ± 1.

Table 3.6 compares the determined rate constants to the values obtained by Plumb and Ryan for similar experimental conditions (at 0.5 torr and 50 W).

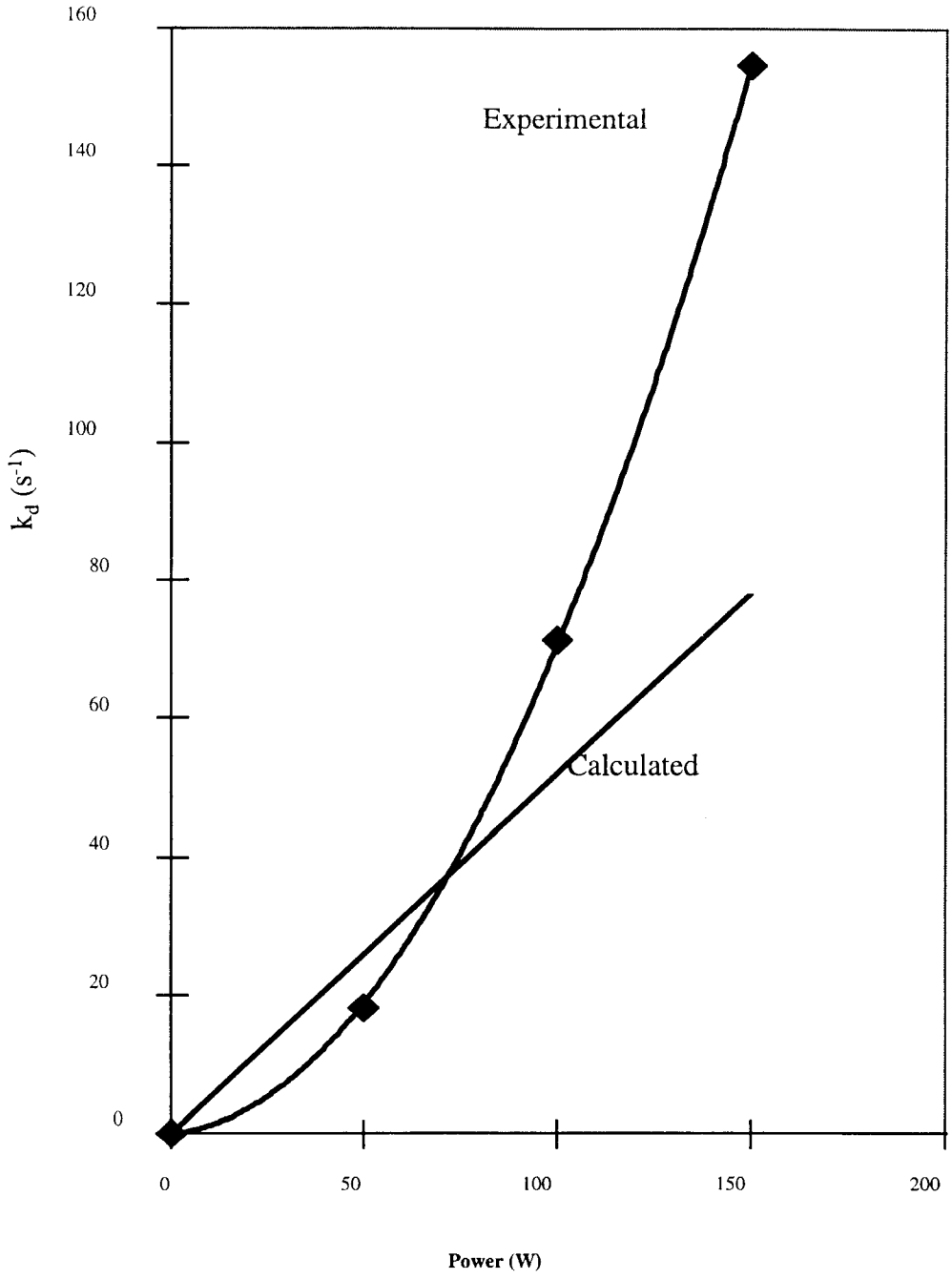

Figure 3.10: Pseudo-first order rate constant as a function of plasma power

Table 3.6: Comparison between literature and determined electron dissociation rate constant

Reaction	Plumb and Ryan	This laboratory
$CF_4 \rightarrow CF_3 + F$	6	5.4
$CF_4 \rightarrow CF_2 + 2F$	14	12.6

3.4.2 Gas Phase Association Reactions:

Species generation and loss in the plasma is done through electron impact dissociation and homogeneous and heterogeneous recombination reactions. The set of homogeneous recombination reactions pertinent to our system as well as their rate constants were adopted from the list of recombination reactions proposed by Plumb and Ryan (Plumb, 1986). Since the given rate constants were either determined experimentally or estimated based on three-body collision theory, it was not judged necessary to attempt to either re-evaluate or recalculate them.

3.4.3 Wall effects:

In the original model, Plumb and Ryan have neglected the wall recombination of the oxygen atoms (Plumb, 1986). But experimental data from our laboratory have shown that oxygen atom surface recombination is an important phenomenon in our system. Therefore, it was found necessary to include it in the kinetic model. From kinetic theory, the rate constant is expressed as:

$$k_w = \frac{1}{4}\gamma u_0 \qquad 3.16$$

where γ is the wall recombination coefficient and u_0 is the velocity of the oxygen atom given by:

$$u_0 = \sqrt{\left(\frac{8kT}{\pi M_1}\right)} \qquad 3.17$$

where M_1 is the atomic mass of oxygen. The wall recombination coefficient of atomic oxygen has been shown in the literature to vary from $1.6 \cdot 10^{-4}$ and $1.4 \cdot 10^{-2}$. Experimental data from our laboratory have shown that the O atoms concentration at the exit of the tube in our system was three times greater at 90 sccm than it is at 30 sccm. It suggests that at a low volumetric flow rate, O atoms wall recombination affect the gas phase concentration in the effluent gas. Based on that information, the wall recombination coefficient γ is estimated to be approximately 10^{-3}.

3.5 Transport processes: Dependency of the Rate Constant on Pressure

In a low strength electric field, very few electrons will possess enough energy to participate in inelastic collisions and create reactive species. Thus, the average electron energy is mainly dependent on the strength of the electric field E, and the pressure *p* of the system and can be described by the following simple relationship (Bell, 1974):

$$\langle \varepsilon \rangle \alpha \frac{E}{p} \qquad 3.18$$

The efficient transfer of energy from the electric field to the electrons is an important parameter in discharge plasmas and has prompted the use of a microwave plasma. A change in pressure affects the EEDF and the electron impact dissociation rate constants.

In this section, the model is developed to estimate the change in average electron energy with pressure.

Under steady state operating conditions, the loss and creation of charged particles by diffusion and ionization maintains the discharge. A general electron balance on the discharge leads to the following equation:

$$\frac{\partial n_e}{\partial t} + \nabla \cdot (n_e u) = n_e \cdot \nu_i \qquad 3.19$$

where ν_i is the ionization frequency, u the velocity of electrons. The first term on the left-hand side represents the rate of electron accumulation in the discharge with time and the second term describes the change of electron density resulting from convection. The term on the right hand side is the rate of electron generation by electron-molecule collisions in the plasma.

The electron momentum balance can be written as follows:

$$\frac{\partial (n_e mu)}{\partial t} + \nabla \cdot (n_e muu) = -\nabla p - n_e eE + n_e mu\nu_m \qquad 3.20$$

where m is the mass of the electron and ν_m the momentum collision frequency. The first term on the right hand side is pressure force, the second term is for the effect of the electric field on the charged species and the third term describes electron-molecule collisions. The first term on the left-hand side is for accumulation of momentum with time and the second term is for changes of momentum by convection.

At steady state and ignoring inertial effects, the left-hand side goes to zero. Solving Equation 3.20 for the flux:

$$n_e u = \frac{-\nabla p}{m\nu_m} - \frac{n_e eE}{m\nu_m} \qquad 3.21$$

Applying the ideal gas law and assuming that the system is isothermal

$$n_e u = -\frac{kT\nabla n_e}{m\nu_m} - \frac{n_e eE}{m\nu_m} \qquad 3.22$$

The above equation can be rewritten as:

$$n_e u = -D_e \nabla n_e - \mu_e E \qquad 3.23$$

where the diffusion coefficient D_e and the mobility μ_e are defined as:

$$D_e = \frac{kT}{m\nu_m} \quad and \quad \mu_e = \frac{n_e e}{m\nu_m}$$

At steady state, the continuity Equation 3.19 becomes:

$$\nabla \cdot \left(-D_e \nabla n_e - \mu_e E\right) = n_e \nu_i \qquad 3.24$$

The ion flux must equal the electron flux in order to maintain a zero flux current at the boundaries:

$$-D_e \nabla n_e - \mu_e E = -D_i \nabla n_i - \mu_i E \qquad 3.25$$

Solving for E:

$$E = \frac{D_i - D_e}{\mu_i - \mu_e} \nabla n_e \qquad 3.26$$

Substituting for E in the continuity equation gives:

$$\nabla \cdot \left(\frac{-\mu_e D_i - \mu_i D_e}{\mu_i - \mu_e} \right) \nabla n_e = n_e \nu_i \qquad 3.27$$

Defining the ambipolar diffusivity as:

$$D_a = \frac{-\mu_e D_i - \mu_i D_e}{\mu_i - \mu_e} \tag{3.28}$$

The continuity equation becomes:

$$D_a \nabla^2 n_e = n_e \cdot \nu_i \tag{3.29}$$

For a one-dimensional cylindrical geometry shown in Figure 3.2, Equation 3.27 becomes:

$$D_e \left[\frac{1}{r} \frac{\partial}{\partial r} \left(r \frac{\partial n_e}{\partial r} \right) \right] + n_e \cdot \nu_i = 0 \tag{3.30}$$

with the following boundary conditions:

$$\frac{\partial n_e}{\partial r} = 0 \qquad \text{at} \qquad r = 0$$

$$n_e = 0 \qquad \text{at} \qquad r = R$$

where R is the radius of the cylinder.

The electron density distribution is obtained by solving Equation 3.27 and given by:

$$n_e = n_{eo} \cdot J_0 \left(\frac{2.44r}{R} \right) \tag{3.31}$$

in which J_0 represents the zeroth order Bessel function and

$$\frac{\nu_i}{D_a} = \left(\frac{2.4}{R} \right)^2 \tag{3.32}$$

$$\nu_i = k_i \cdot N \tag{3.33}$$

and N is the total gas density.

Combining Equations 3.31, 3.32, 3.33 and the ideal gas law leads to the following expression:

$$p = \left(\frac{2.4}{R}\right)^2 \cdot D_a \cdot \frac{kT}{\int_0^\infty 1.034\sqrt{\frac{2}{m}}\frac{\varepsilon}{\langle\varepsilon\rangle^{3/2}}\exp\left(-0.545\frac{\varepsilon}{\langle\varepsilon\rangle}^2\right)\sigma_i d\varepsilon} \qquad 3.34$$

or

$$p = \frac{const}{\int_0^\infty \frac{\varepsilon}{\langle\varepsilon\rangle^{3/2}}\exp\left(-0.545\frac{\varepsilon}{\langle\varepsilon\rangle}^2\right)\sigma_i d\varepsilon} \qquad 3.35$$

with $const = \left(\frac{2.4}{R}\right)^2 \cdot D_a \cdot \frac{kT}{1.034\sqrt{\frac{2}{m}}}$

Equation 3.35 describes the change of the average electron energy as a function of pressure and can be used with the appropriate cross-sectional data to determine the average electron temperature at different pressure given its value for a specific pressure. For our rate calculations, an electron energy of 5.9 eV at 0.5 torr is used. Table 3.7 shows the electron energy as a function of pressure. Table 3.8 gives the rate constants considered in the simulation at 0.2 and 0.8 torr.

Table 3.7: Average electron temperature as a function of pressure.

Pressure (torr)	$\langle\varepsilon\rangle$ (eV)
0.2	6.65
0.5	5.90
0.8	5.46

Table 3.8: Pseudo-first order rate coefficients used in the simulation.

Reaction	Rate coefficient at 0.2 torr and 50 W	Rate coefficient at 0.2 torr and 100 W	Rate coefficient at 0.2 torr and 150 W
$CF_4 \rightarrow CF_3 + F$	15	57	85
$CF_4 \rightarrow CF_2 + 2F$	36	132	200
$F_2 \rightarrow 2F$	51	189	286
$COF_2 \rightarrow COF + F$	51	189	286
$CO_2 \rightarrow CO + O$	51	189	286
$O_2 \rightarrow 2O$	25	92	138
$O_2 \rightarrow O + O(1D)$	11	39	59

Reaction	Rate coefficient at 0.8 torr and 50 W	Rate coefficient at 0.8 torr and 100 W	Rate coefficient at 0.8 torr and 150 W
$CF_4 \rightarrow CF_3 + F$	4	14	21
$CF_4 \rightarrow CF_2 + 2F$	9	33	50
$F_2 \rightarrow 2F$	13	47	72
$COF_2 \rightarrow COF + F$	13	47	72
$CO_2 \rightarrow CO + O$	13	47	72
$O_2 \rightarrow 2O$	6	23	35
$O_2 \rightarrow O + O(1D)$	2	10	15

CHAPTER 4

METHOD OF SIMULATION

A reacting plasma can be modeled through solving the continuity equations for each species, the momentum conservation equation for the fluid flow and the energy balance for the gas temperature. In order to develop such a model, it is necessary to determine the identity of the active chemical species as well as the rates and mechanisms of the reactions between them. The earlier part of the report focused on defining an adequate gas phase chemistry model for a CF_4/O_2 microwave generated plasma. The above quoted governing equations are then solved simultaneously in order to obtain a numerical solution. The large number of chemical species and reactions involved makes the analytical solution untractable. Thus, this problem is solved using Computational Fluid Dynamics (CFD). Fluent, a CFD tool that uses the control volume technique to solve the governing equations is chosen.

The following paragraphs describes the solution procedure utilized in Fluent and its applicability to a plasma reacting flow.

4.1 Governing equations:

The general form of conservation of a physical quantity A is obtained when a balance is performed over a microscopic control volume and given by:

$$(\text{Input of A}) - (\text{Output of A}) + (\text{Generation of A}) = (\text{Accumulation of A}) \quad 4.1$$

When the physical quantity A represents mass, momentum and heat, Equation 4.1 yields

the equation of continuity, the equation of motion and the equation of energy conservation respectively, which are equations that correlate concentration, pressure, velocity and temperature. These equations are described as they apply to the model being considered with x_i representing the three position coordinates and u_i the velocity in the three directions.

4.2 The Conservation of Mass:

The general mass conservation equation is obtained by performing an overall mass balance on the control volume and describes the rate of change of density resulting from the changes in the mass velocity vector. The fluid property needed to solve this equation is density ρ. The mass density was calculated by means of the ideal gas law. The use of the ideal gas equation of state is appropriate since the processes considered occur at low pressure.

$$\frac{\partial \rho}{\partial t} = -\frac{\partial (\rho u_i)}{\partial x_i} \qquad 4.2$$

$$\rho = \frac{pM}{RT} \qquad 4.3$$

where p is pressure, M is the molecular weight, R is the ideal gas constant and T, the fluid temperature.

4.3 The Conservation of Species Equations

The species conservation equation is obtained when the overall mass conservation equation is applied to individual species in the fluid. It describes changes in species' concentration due to diffusion and convection mass flux as well as chemical reactions.

$$\frac{\partial(\rho\ m_{i'})}{\partial t}+\frac{\partial(\rho u_{i'} m_{i'})}{\partial x_i}=\frac{\partial(J_{i'i})}{\partial x_i}+S_{i'} \qquad 4.5$$

where m_i is the mass fraction of species i, $J_{i'i}$ is the diffuse flux and S_i is the rate of production due to chemical reaction. The diffusion flux, $J_{i'i}$ is defined as:

$$J_{i'i}=-\rho D_{i',m}\frac{\partial m_{i'}}{\partial x_i}-D_{i'}^{T}\frac{i}{T}\frac{\partial T}{\partial x_i} \qquad 4.6$$

where $D_{i',m}$ is the diffusion coefficient for species i' in the gas mixture and $D_{i'}^{T}$ is the thermal diffusion coefficient for species i'. The transport model contains 16 species among which only Ar is inert. Due to limit in computational requirements, only 12 were considered in the calculation of the multicomponent diffusion coefficient: O_2, CF_4, O, F_2, F, CO_2, CO, COF_2, COF, CF_3, CF_2 and Ar. The binary diffusion coefficients are estimated using Chapman-Enskog kinetic theory with the Lennard-Jones parameters.

The reactions rates are computed as the sum of the reactions sources over the k reactions that each species i' participate in.

$$R_{i'}=\sum_{k}R_{i',k} \qquad 4.7$$

The rate of creation of species i' is described by an Arrhenius type kinetic rate expression:

$$R_{i',k}=-\nu_{i',k}M_{i'}T^{\beta_k}A_k\prod_{j'\text{reactants}}C_{j'}^{\nu_{j'k}}\exp\left(\frac{-E_k}{RT}\right) \qquad 4.8$$

where

$\nu_{i',k}$ = molar stoichiometric coefficient for species i' in reaction k
$M_{i'}$ = molecular weight of species i'
β_k = temperature exponent
A_k = pre – exponential factor
$C_{j'}$ = molar concentration of each reactant species j'
$\nu_{j'k}$ = exponent on the concentration of reactant j' in reaction k
E_k = activation energy for the reaction

For the reactions defined in our model, E_k and β_k were set to zero, since the main assumption of the model is that the rate constants are independent of temperature and constant throughout the domain.

Since the model assumes that the flow is isothermal, the energy conservation equation was not solved for.

4.4 The Conservation of Momentum:

The motion of a fluid is described by the conservation of momentum equation or the Navier-Stokes equation, which is obtained by performing a force balance on the control volume. This formulation assumes Newtonian behavior of the gases.

$$\frac{\partial(\rho u_i)}{\partial t}+\frac{\partial(\rho u_i u_j)}{\partial x_j}=-\frac{\partial p}{\partial x_i}+\frac{\partial}{\partial x_i}\left[\mu\left(\frac{\partial u_i}{\partial x_j}+\frac{\partial u_j}{\partial x_i}\right)\right]+\rho g_i+F_i \qquad 4.4$$

The left-hand side expressions correspond, respectively, to the accumulation of momentum with time and change in the velocity. The first term on the right hand side expression accounts for pressure force, the second term describes sheer stress and the third term is gravity.

The viscosity is calculated from Chapman-Enskog kinetic theory for the feed mixture of O_2, CF_4 and Ar and assumed constant over the domain.

4.5 Equations Solving

The set of differential equations which constitute the governing equations. With boundary conditions, these equations are solved numerically by Fluent using the control volume technique. It consists in dividing the flow domain into discrete control volumes, converting the differential conservation equations into algebraic equations for each control volume and solving the discretized equations.

4.6 Discretization

The geometry was based on direct measurement of the dimensions of the system displayed in Figure 3.1. Two grids were set-up, one consisted of the geometry displayed in Figure 3.2 while the second consisted of the quartz tube and the reactor chamber and was defined as a two dimensional axisymmetric cylindrical region. The subsequent grid generated consists of 5045 computational cells (Figure 4.1). The flow area was divided into rectangular areas; each block represents a cell and the complete network of cells is called the mesh. Since, flow through the pipe is axisymmetric, only a 2-dimensional representation of half of the pipe needs to be modeled. Boundary conditions are applied to the cells that are on the borders of the mesh while the remaining cells are live cells governed by the governing conservation equations. The inlet boundary conditions, pressure, temperature and feed composition were specified based on the case of interest

(e.g. at 0.5 torr, 298 K and 75% O_2/ 20% CF_4/ 5% Ar).

In the present model, a second type of live cells was defined to represent the plasma cavity. The main characteristic of plasma downstream etch system is that active chemical species are created in the plasma cavity before being transported by flow to the processing chamber. For modeling such a system, it is necessary to make the assumption that the electrons, which initiate and sustain the dissociation reactions, have uniform density and energy in the plasma region and that the electron density falls off to zero outside the plasma. It is therefore necessary to specify reactions that occur only in the plasma cavity; in the afterglow, the electron impact dissociation reactions can not occur.

The differential equations are integrated about each control volume and converted into algebraic equations that conserve each quantity on a control volume basis. The volume integration used in Fluent is illustrated below for the two-dimensional continuity equation.

The value of the entire cell is represented by a single value stored at the center of the cell. The two-dimensional differential equation for continuity under state conditions yields:

$$\frac{\partial(\rho u)}{\partial x}+\frac{\partial(\rho u)}{\partial y}=0 \qquad 4.9$$

which can be integrated about a control volume:

$$\int_{\text{volume},V}\frac{\partial(\rho \mathrm{u})}{\partial \mathrm{x}}\mathrm{dV}=\int_{\mathrm{A}}\rho \mathrm{u}\cdot\mathrm{dA} \qquad 4.10$$

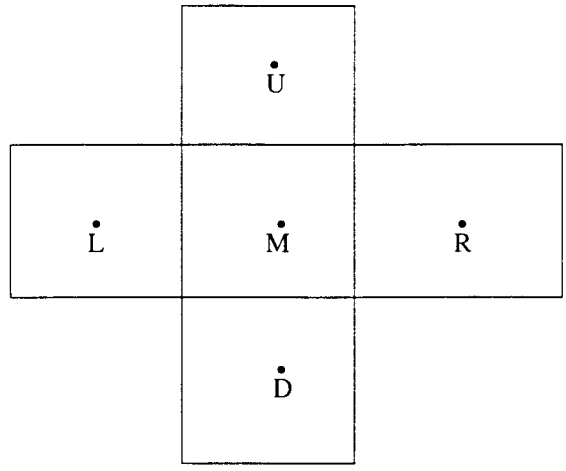

Figure 4.1: Nodal Representation in numerical scheme.

If one considers the distance between the nodes to be Δx in the x direction and Δy in the y direction, the discretization of Equation leads to Equation 4.11:

$$\frac{u_x^R - u_x^L}{\Delta x} + \frac{u_y^U - u_y^D}{\Delta y} = 0 \qquad 4.11$$

The volume integration of Equation 4.9 has led to Equation 4.11, an algebraic equation, which can be solved if the unknown velocity at the control volume faces is related to its stored value at the center of the control volume. Interpolation schemes are used to relate the face values of the unknown u to the value at the control volume center.

One interpolation scheme is the power law scheme, which is based on the dimensionless Peclet number, Pe. Pe is the ratio of the convective transport to diffusion transport of a physical property.

The power law interpolation scheme applied to the above two-dimensional continuity equation is:

$$\frac{u_x^{face} - u_x^{M}}{u_x^{R} - u_x^{M}} = \frac{\exp\left(Pe \cdot \frac{x}{L}\right) - 1}{\exp(Pe) - 1} \qquad 4.12$$

The term x/L is the ratio of the distance from the face to node M and L is the distance from node R to node M. When diffusion dominates, Pe = 0, u can be approximated by a simple linear average between the values at x=0 and x= L. When convection dominates, the face value can be approximated by its upstream value. When Pe has an intermediate value, the interpolated value of u has to be derived by applying the power law scheme described above.

Higher order interpolation schemes compute the face value of the unknown parameter by adding a third cell upstream. The use of higher order interpolation schemes provides greater numerical accuracy but can be subject to numerical instabilities.

The conversion of the differential conservation equations into algebraic equations using the control volume technique generates a set of algebraic equations. These equations are solved by using the Line-Gauss-Sidel iterative scheme, which solves the set of equations either column by column, row-by-row or a combination of both. A solution is obtained when the sum of the errors for the cells is less than the maximum derived error, which ranges between 10^{-3} and 10^{-6}.

CHAPTER 5

RESULTS AND DISCUSSION

The purpose of the present study is to develop a kinetic model, which describes the gas phase chemistry of the CF_4/O_2 discharge plasma and afterglow in our laboratory. Chapter 3 outlined the plasma model formulation by describing the reaction pathway (displayed in Figure 3.3) and defining the kinetic parameters of the chemical reactions (electron impact dissociation and gas phase recombination reactions). In order to compare the model's prediction to the experimental data, governing fluid equations (conservation of mass, momentum and species equations) are applied to the discharge plasma and afterglow, generating a set of differential equations, which can be solved by computational fluid dynamics as described in Chapter 4. In the present chapter the solution to the fluid equations are discussed. First model parameters and results from the literature are used to confirm the validity of this approach. Then simulation results are compared with experimental measurements from our laboratory. Finally, the examination of the effects of plasma power, residence time and system pressure on the species concentration and distribution in the system is discussed.

5.1 Comparison with other Studies in the Literature

In order to evaluate the validity and accuracy of the computational fluid dynamics (CFD) simulations, the first set of runs were conducted under conditions similar to those reported in the literature (Plumb, 1986). The literature calculation results were obtained using a differential equation solver program called Sock. This program (Davies, 1986)

uses the Gear numerical technique to solve the set of differential equations obtained by applying the general fluid conservation laws to the system. Plumb and Ryan have considered in their calculation a larger set of chemical reactions (45 reactions); however, their model is one-dimensional, therefore, ignored the effect of diffusion. Figures 5.1 and 5.2 plot the concentration of the various species in the reactor as a function of distance along the tube (the simulated values were collected along the centerline), for a volumetric flow rate of 70 sccm which corresponds to a nominal residence time of 7 ms. In part (a) of these figures, the results from our simulations are reported; part (b) plots those from Plumb and Ryan. Figure 5.1 shows results for a gas mixture of 25 mole % O_2 and 75 mole % CF_4 in the feed while Figure 5.2 are for a 75 mole % O_2 and 25 mole % CF_4.

The analysis of Figures 5.1 and 5.2 shows that the CFD simulation results reproduce qualitatively the computed concentration profiles presented in the literature. These results can be interpreted in terms of the chemistry model described in Figure 3.3 where CF_3, CF_2 and COF are seen as short-lived intermediate reactive species. Their concentrations reach a maximum in the plasma region before rapidly falling to zero in the afterglow. The concentration of CF_2 in the discharge is far greater than CF_3 due to the selected branching ratio of CF_4 electron impact dissociation and the fast recombination of CF_3 with F atoms.

Figures 5.1 and 5.2 also show how the distribution of the major stable products, COF_2, CO_2 and CO, depends on the feed composition. At 75 mole % CF_4 (Figure 5.2), the high concentration of F atoms strongly influences the fast recombination reaction of CF_3 and F atoms and limits the net CF_4 dissociation. The O atoms produced by electron

impact reactions are almost completely consumed through reactions with CF_2 to form COF, which in turn react with the predominant F atoms to form COF_2. Because of the low concentration of atomic oxygen, the reaction of COF with F atoms to produce COF_2 is more probable than the reactions of COF with O atoms to form CO_2 and CO, thus, COF_2 is the dominant stable product in the post-discharge region. With 25 mole % CF_4 in the feed, the resulting concentration profiles are notably different from the previous case. The O atom concentration increases by two orders of magnitude and becomes almost equal to that of F atoms throughout the reactor. Again, CF_2 reacts with O atoms to form COF but in this case there is sufficient O to lead to CO_2 and CO instead of COF_2.

This study predicts lower concentrations of CF_2, O and CO and higher concentrations of COF_2, COF, CF_3 and C_2F_6 than those from the literature. The observed differences in the concentration of the intermediate species (COF, CF_3 and CF_2) apparently account for the differences seen in the concentration of the major stable products. For example, based on the selected chemistry model, a higher concentrations of COF and lower concentration of O in a CF_4 dominated environment would explain the higher concentration of COF_2 and lower CO_2 and CO concentrations obtained in our calculations. Furthermore, CF_3O_2 is an additional species seen in Figure 5.2 (b) and not considered in our simulation calculations. As explained earlier, the literature calculations considered the full set of the 45 chemical reactions originally proposed (Plumb, 1986), while the CFD computations considered only the reduced set of 14 reactions shown in Table 3.2. CF_3O_2 is a product of the reaction of CF_3 with O_2, therefore not accounting for this reaction results in higher concentrations of CF_3 and C_2F_6. Similar differences can be

observed in Figure 5.1. The difference in the concentration of the intermediate species appears to be more significant. The literature calculations predict the concentration of CF_2 to be as high as $9 \cdot 10^{12} \frac{atoms}{cm^3}$ while our results show it to be near $5 \cdot 10^{12} \frac{atoms}{cm^3}$. The concentration of COF is also lower resulting in shifts in the predicted concentrations of CO_2, CO and COF_2. The concentration and concentration profiles of the reactant CF_4 and O_2 and the products F, F_2 and CO_2 resulting from the CFD simulations are in general good agreement with those obtained in the literature. For the reactive intermediates, diffusivity and grid size can contribute to the difference. However, the direct comparison of the plots suggests that species generation and stable product formation occur at a faster rate in our simulations than it does in the literature ones. In Figure 5.1, the final concentration of F is the same for both computed results, but the slope of the concentration with position in the plasma cavity is much greater for the literature values. And similar observations can be made for other intermediate and active species.

Overall, the agreement between literature and our results is good suggesting that the application of computational fluid dynamics to the discharge plasma is appropriate and can provide reasonable qualitative and quantitative information on our system.

5.2 Comparison with the Experimental Results

Figure 5.3 compares simulated values of CF_4 conversion downstream of the plasma to the conversions obtained by the mass spectrometer in our laboratory.

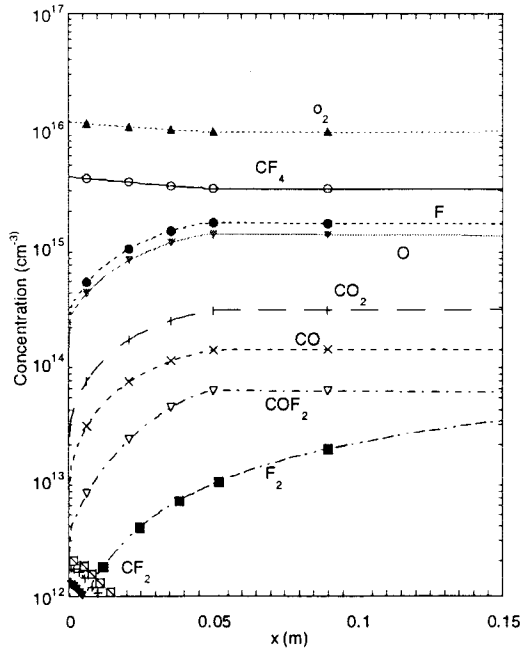

(a)

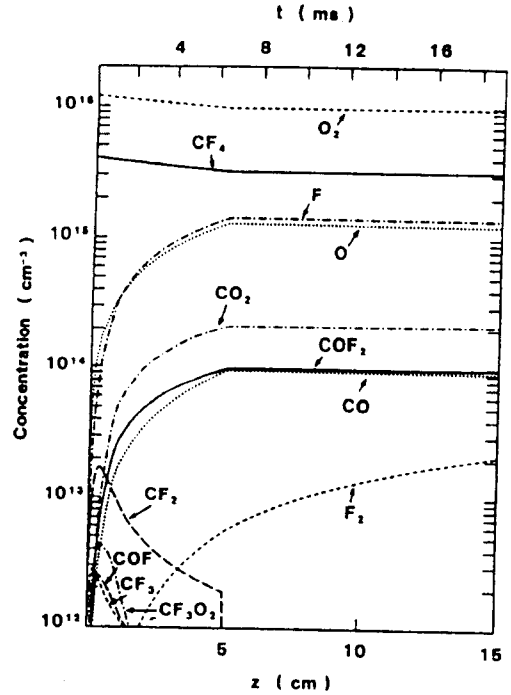

(b)

Figure 5.1: Computed Concentrations for 25% CF_4/75 % O_2 plasma as function of the distance x from the entry of gas in the plasma at 0.5 torr and 70 sccm. (a = our data while b = literature data).

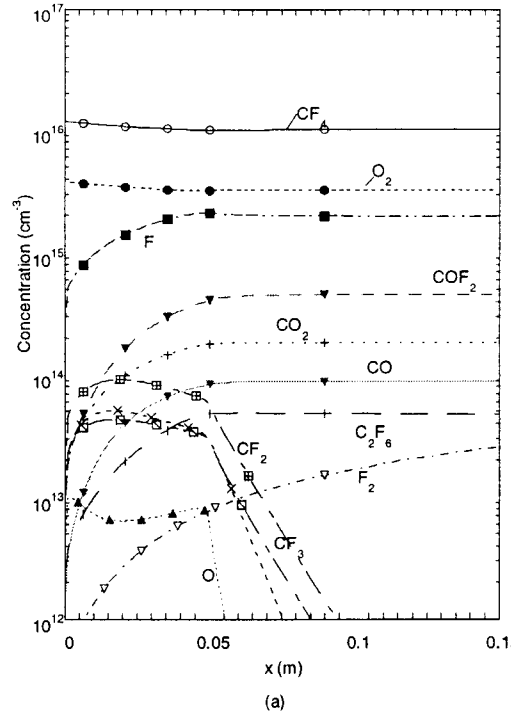

(a)

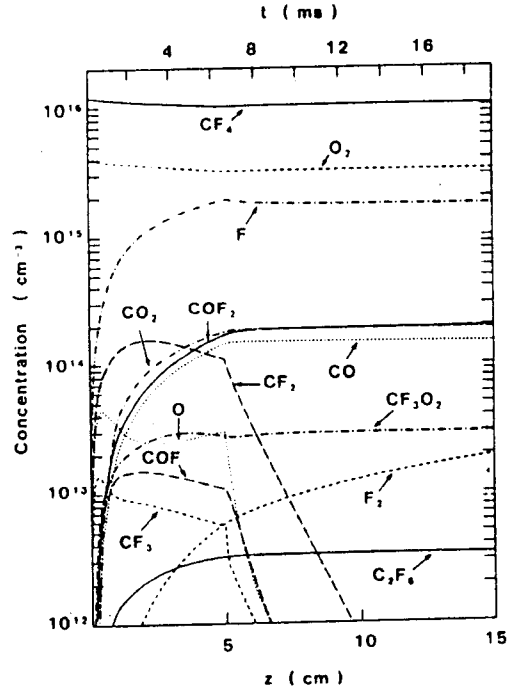

(b)

Figure 5.2: Computed Concentrations for 75% CF_4/25 % O_2 plasma as function of the distance from the entry of gas in the plasma at 0.5 torr and 70 sccm. (a = our data , b = literature data).

Details of the measurements are presented elsewhere (Hsu, 1997). A gas mixture of 75% O_2, 20% CF_4 and 5% Ar at 0.5 torr was used. Flow rates and plasma power varied from 20 to 100 sccm and 50 to 150 W, respectively.

The model reproduces the general trends of the experimental data: conversion increases with power and residence time. However, the simulation data tends to predict too high a conversion at short residence times and too low a conversion at long residence times. In other words, the slope of the simulated data in Figure 5.3 should be steeper to better fit experimental data. There are two possibilities, which can account for this discrepancy. The discharge structure is assumed to be independent of flow rate. Lower flow rates, and more dissociation, may change the electron energy distribution or the electron number density. This explanation is consistent with the fact that the slope for the experimental data increases with power. An alternative hypothesis is that the discrepancy may be due to inaccuracies in the rates of the homogeneous reactions. For example, the recombination of CF_3 and F may be too fast ($k = 1.3 \cdot 10^{-11} cm^3 s^{-1}$), in fact the rate at which CF_3 recombines with F is thirty times that of CF_2 and F. Thus, the majority of CF_3 produced by electron impact dissociation quickly recombines with F to reform CF_4. This mechanism would underestimate total conversion at larger conversions.

Figure 5.4 compares simulated and experimental distributions of stable carbon containing products, CO_2, CO and COF_2, for the 100 W data presented in Figure 5.3. In both cases, CO_2 is the major stable product in the outlet stream; its concentration increases with plasma power (not presented) and residence time. At short residence time, the simulation overpredicts CO_2 concentration while at long residence time, it

underpredicts the CO_2 concentration. Again these data indicate that the electron energy distribution or electron number density may be a function of residence time. In all cases, the model underpredicts CO concentration and overpredicts COF_2 concentration. These results indicate that the quantification of the homogeneous reactions or the branching ratio of CF_4 decomposition by electron impact dissociation may need to be adjusted. The trend with plasma power is expected since an increase in the plasma power in the model corresponds to an increase in the rate constant of the electron impact dissociation reactions of CF_4 in the plasma. COF is the main intermediate species, which is ultimately converted to either CO_2 and CO or COF_2. An over estimation of the rate coefficient of the reaction of COF with F to form COF_2 may be translated into a decrease in the formation of the other stable products CO_2 and CO, and account for their low relative concentrations in the simulation data.

Considering the complex nature of the plasma environment and the significant number of assumptions made in order to obtain the kinetic information pertinent to our system as well as the difficult experimental protocol, it is not surprising that there are quantitative discrepancies between experiment and simulation. However, the model describes the gas phase chemistry of the CF_4/O_2 discharge plasma well enough to predict the general trends of the species distribution. Moreover, it provides a way of thinking about the complexities of the reactive plasma environment.

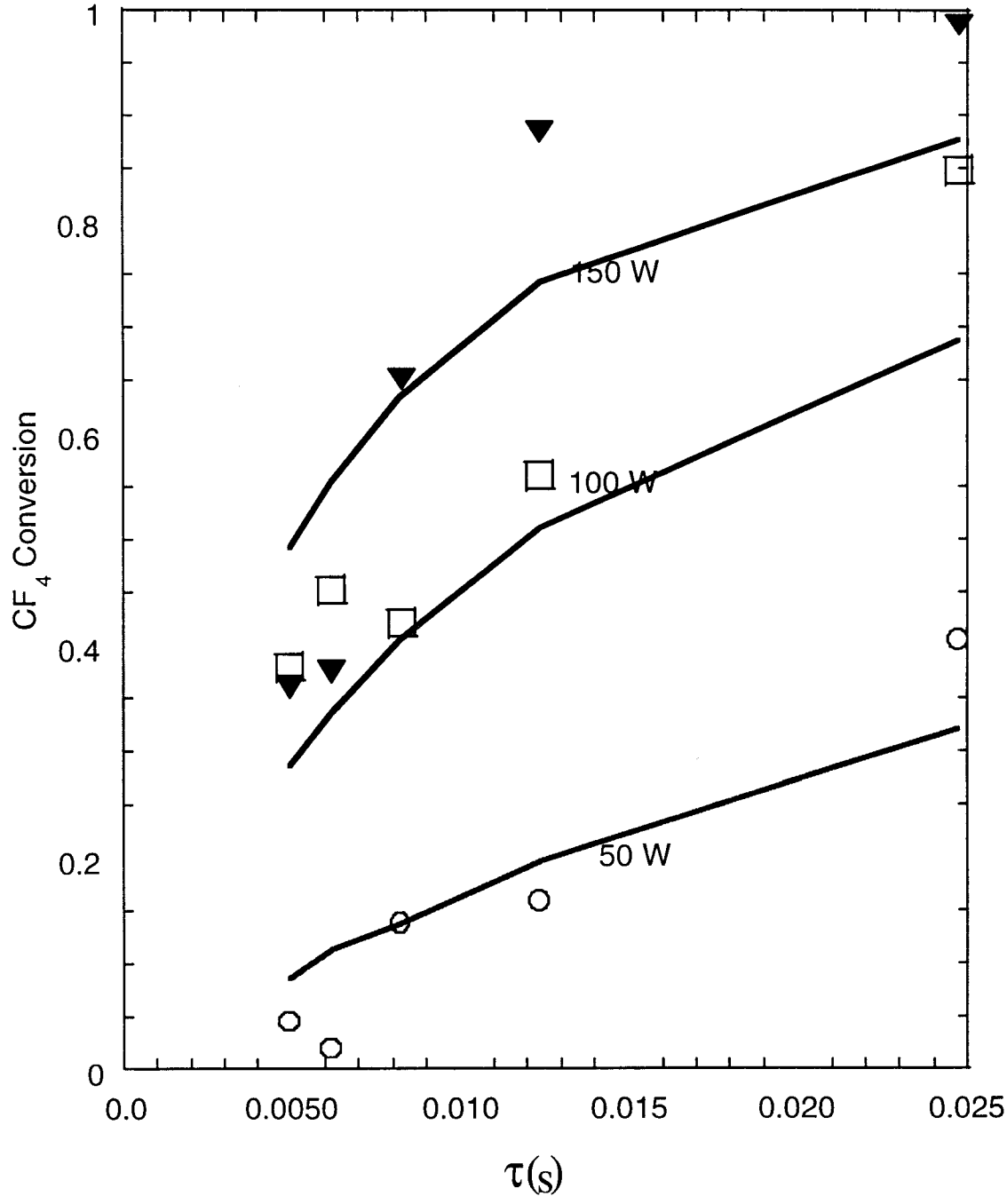

Figure 5.3: Comparison of experimental and computer simulation CF_4 conversion for 20%CF_4 /5% Ar /75% O_2 gas mixture. Total pressure = 0.5 torr, flow rates = 20, 40, 60, 80 and 100 sccm. The lines without data represent the simulation results while the symbols represent the experimental data.

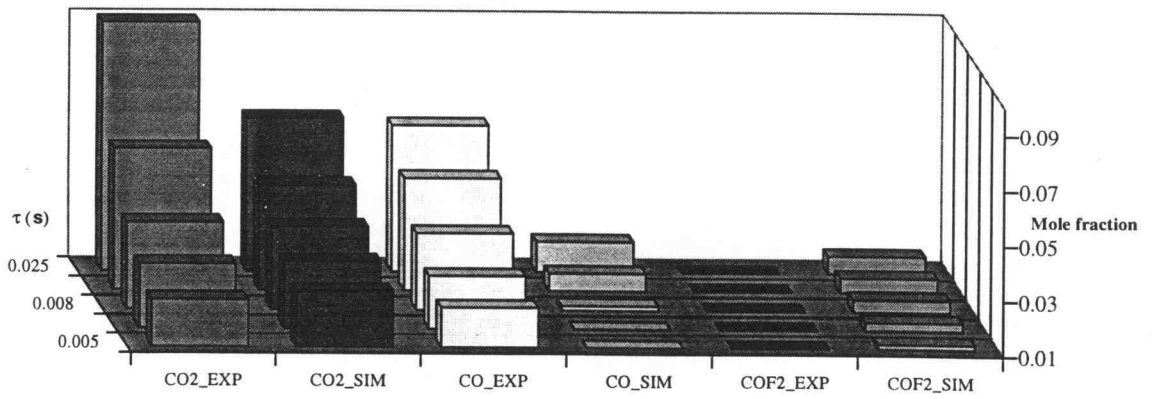

Figure 5.4: Comparison of experimental and simulation product distribution for a 20% CF_4/ 75% O_2/5% Ar gas mixture at 0.5 torr and 100 W.

5.3 Conversion and Compositions at the Afterglow Exit

The effect of both plasma power and inlet gas mixture composition on the CF_4/O_2 discharge plasma CF_4 conversion and product distribution is presented in Figures 5.5-5.8. In each of these figures, the two volumetric flow rates studied, 20 and 100 sccm, are represented by the labels (a) and (b), respectively. The simulations are performed 0.3 m downstream of the plasma at the exit of the afterglow region with a pressure of 0.5 torr. The plasma power varies from 50 to 150 W.

Figure 5.5 displays the simulated CF_4 conversion as a function of mole % CF_4 in the feed. At a fixed gas composition, CF_4 conversion is, in most cases, proportional to plasma power except at 20 sccm and high power where there is an apparent saturation of CF_4 decomposition. For a given power and flow rate, the variation of CF_4 conversion with feed composition falls into two regimes. In the oxygen rich regime, 0 to 25 mole % CF_4, the conversion is only weakly dependent on CF_4 concentration (the linear

dependency has a relatively flat slope). At higher concentrations, above 25 mole % CF_4, CF_4 conversion decreases linearly as CF_4 concentration increases.

Figure 5.6 plots the mole fraction of the carbon containing species (CO_2, CO and COF_2) as a function of mole % CF_4 in the feed. CO_2 is the major product in the oxygen rich region (roughly less than 50 mole % CF_4) while COF_2 becomes the major product in the CF_4 rich region (roughly greater than 50 mole % CF_4). Conversely, CO is a minor product, which never becomes the dominant carbon containing species downstream of the plasma. Furthermore, the concentration profile of CO follows the same trend as CO_2 with a maximum concentration obtained in the oxygen rich region. The variations of CO_2 and CO are proportional to changes in plasma power when other conditions, such as mole % CF_4 in the feed and flow rate, are identical. However, at 20 sccm and 150 W, there is an apparent saturation of the production of CO_2 (shown in Fig. 5.6.a). This behavior is similar to that presented in Fig. 5.5.a. Similarly, the concentration of COF_2 is proportional to plasma power in the CF_4 rich regime. In the oxygen rich regime where it is a minor product, the mole fraction of COF_2 at 150 W is actually lower than the one observed at 100 W. Furthermore, the concentration of CO_2 increases linearly as the feed concentration in CF_4 is increased from 0 to 25 mole %. At higher CF_4 concentrations, the CO_2 concentration profile changes with flow rate. At 20 sccm, the concentration of CO_2 decreases with increasing CF_4 concentration. At 100 sccm, it increases with a lower slope than before with mole % CF_4 (from 25 to 50 mole %) before rapidly declining thereafter. The COF_2 concentration has a dramatic increase in slope, which starts at 25 mole %, just where the CO_2 concentration behavior changes.

Figure 5.7 plots the mole fraction of atomic fluorine as a function of mole % CF_4 in the feed. The concentration profiles follow a symmetric pattern, which reaches a maximum at 50 mole % CF_4. The value of the maximum increases with plasma power. For a given power, F concentration is larger at higher flow rate (lower residence time).

Figure 5.8 plots the mole fraction of atomic oxygen as a function of mole % CF_4 in the feed. The behavior of O is very different than F. The atomic oxygen concentration is highest in the oxygen rich regime but decreases sharply with increasing CF_4 concentration. There is a notable change in the slope of that variation again, at 25 mole % CF_4. The oxygen atom concentration increases with plasma power. In all cases, only a small fraction of O remains above 50 mole % CF_4.

In a CF_4/O_2 glow discharge plasma, CF_4 conversion depends on the electron density, the electron energy distribution function (EEDF) and the nominal discharge residence time. In our model, the number of electrons in the plasma is a function of the plasma power squared and the EEDF is solely dependent on the operating pressure. Therefore, at a given pressure, an increase in power results in the increase of the electron impact dissociation reactions rate coefficients (Figure 3.10). In Figure 5.5, the proportional relationship between power and CF_4 conversion illustrates the effects of the electron density on conversion. Conversion increases as plasma power and electron density increase. For example, in Figure 5.5.a, at 20 sccm and 10 mole % CF_4 in the feed, the CF_4 conversions for 50, 100 and 150 W are respectively, 0.35, 0.7 and 0.9. Clearly at the highest power, CF_4 conversion is saturated. At a given power, the values for CF_4 conversion are lower at 100 sccm (Figure 5.5.a) than at 20 sccm due to the decreased

residence time for electron impact dissociation. If only electron impact dissociation reactions occurred in the plasma, one would expect conversion to be independent of feed concentration and the displayed curves in Figure 5.5 would have a slope of zero, which the O_2 rich regime approaches. The linear dependency of CF_4 conversion on feed composition in the CF_4 rich regime above 25 mole % CF_4, suggests that homogeneous recombination reactions as well as plasma induced reactions affect the chemistry.

In the oxygen rich regime (below 25 mole % CF_4), atomic oxygen is present in large concentrations. Therefore, the majority of the radicals produced by the electron impact dissociation of CF_4 (CF_3 and CF_2) react primarily with atomic oxygen. This is seen in Figure 5.8 where the concentration of oxygen atoms decreases rapidly and linearly with increasing mole % CF_4. The concentration of these radicals, mostly CF_2 because of the CF_4 decomposition branching ratio, is kept low by the homogeneous reactions with O atoms to produce COF. Reactions of the intermediate species COF with atomic oxygen to produce CO_2 and CO are more probable than reactions of COF with atomic fluorine to produce COF_2. Therefore, CO_2 and CO are the major products while COF_2 is seen in low concentrations (Figure 5.6). The linear increase in these products below 25% CF_4 also illustrates that this mechanism is controlling. The low concentration of CF_3 radicals and atomic fluorine limits recombination to form CF_4. Furthermore, because atomic oxygen chemistry dominates, only a small fraction of F is consumed and the concentration of F atoms increases. This is also illustrated in Figure 5.7 where the F atom concentration increases linearly with mole % CF_4 in the feed in this regime.

At 25 mole % CF_4 , the effect of fluorine is comparable to that of atomic oxygen. Reactions of the free radicals with both O and F atoms become important. As the reactions of atomic fluorine with the free radicals become more significant, there is a dramatic increase in COF_2 concentration (Figure 5.6). The reactions of COF with both atomic fluorine and oxygen is also shown by the decrease in both CO_2 and CO concentrations. The effect of the reactions of atomic fluorine with free radicals is further illustrated in Figure 5.7 (by the slower rate of F increase with CF_4 concentration: the relationship is no longer linear) and Figure 5.5 (by the decrease in CF_4 conversion).

Above 50 mole % CF_4 in the feed, virtually all the oxygen atoms are consumed by either gas phase reactions with free radicals or wall recombination to reform O_2 (see Figure 5.8). Therefore, the recombination reactions between COF and atomic fluorine become more important than reactions between COF and O atoms. As a result COF_2 is the major product in the CF_4 rich regime (Figure 5.6) while CO_2 and CO are low in concentration. More importantly, the recombination of CF_3 with F to reform CF_4 becomes the major reaction in the system. Therefore, low CF_4 conversion is achieved and F concentration decreases (Figure 5.8).

5.4 Deconvolution of Plasma Processes and Afterglow Chemistry

The product distribution of a CF_4/O_2 in the system is determined by electron dissociation reactions, occurring in the plasma, and homogeneous and heterogeneous reactions between neutrals in the plasma and downstream of the plasma.

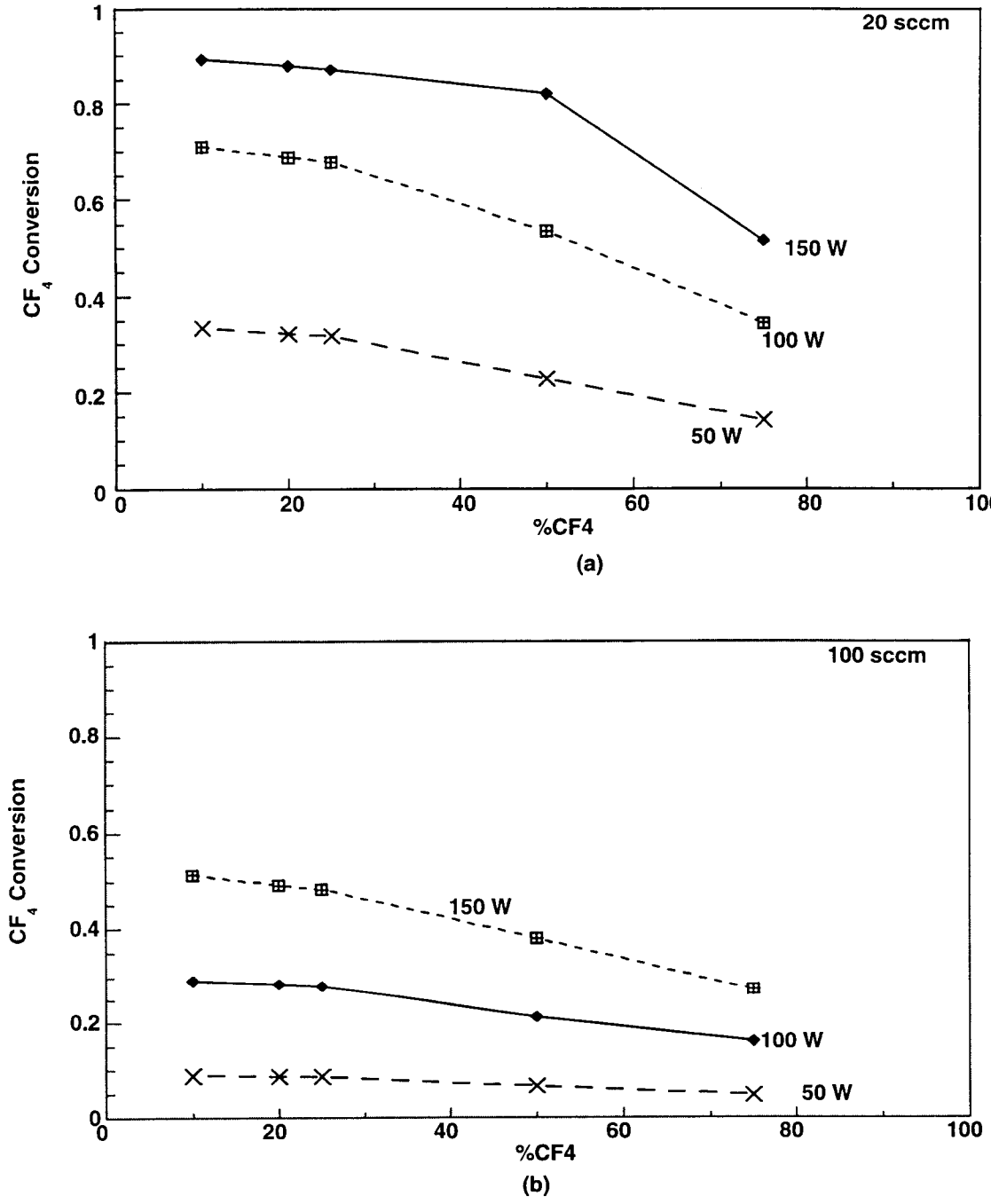

Figure 5.5: Calculated CF_4 conversion as a function of mole % CF_4 in the feed for data collected downstream of the discharge. Total pressure = 0.5 torr, flow rates = 20 and 100 sccm

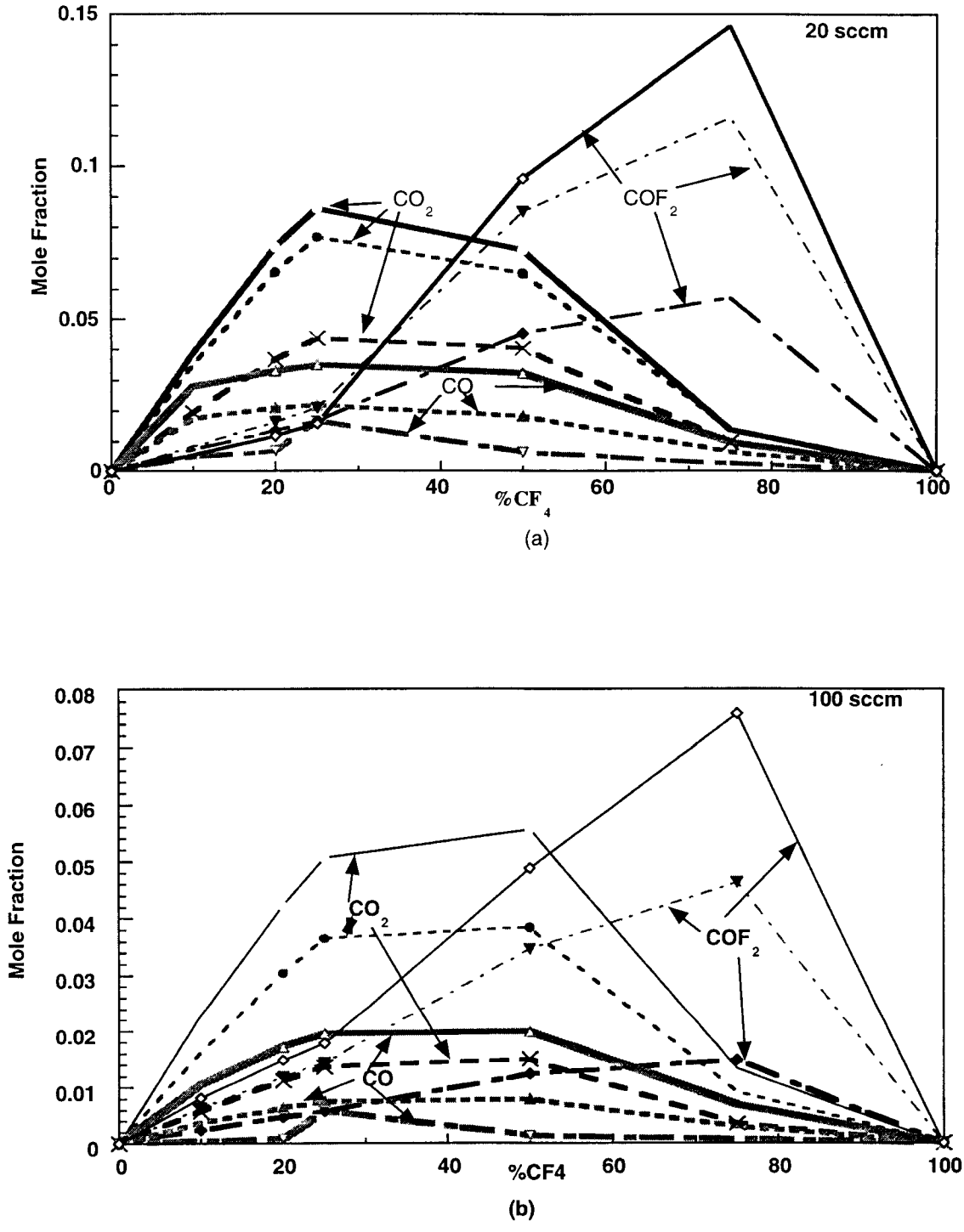

Figure 5.6: Mole fraction of carbon contained species, CO_2, CO and COF_2 as a function of mole % CF_4 concentration in the feed for data collected downstream the plasma. Pressure = 0.5 torr, flow rates = 20 and 100 sccm as indicated.

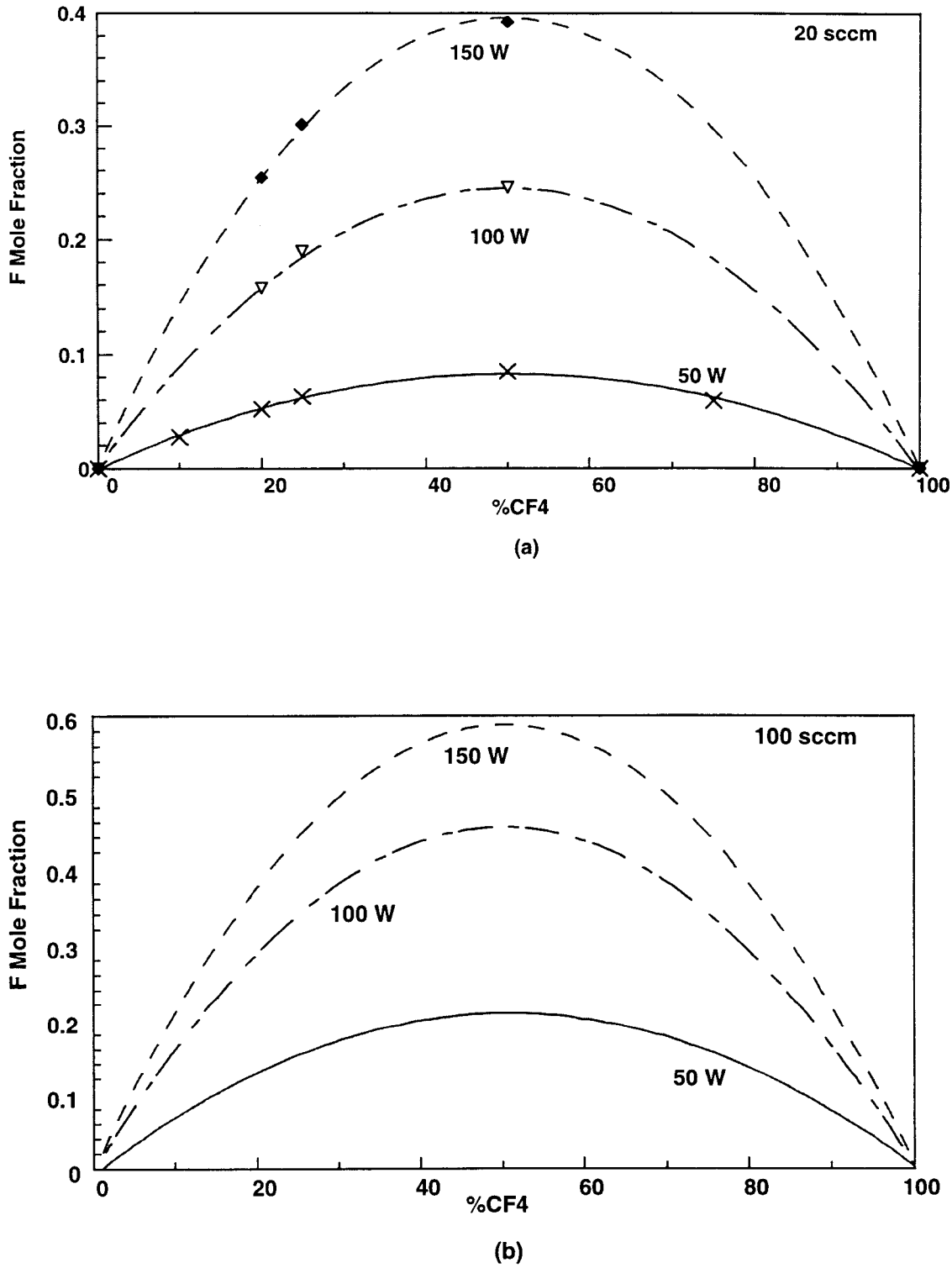

Figure 5.7: Mole fraction of atomic fluorine as a function of CF_4 concentration in the feed. Total pressure = 0.5 torr, flow rates = 20 and 100 sccm

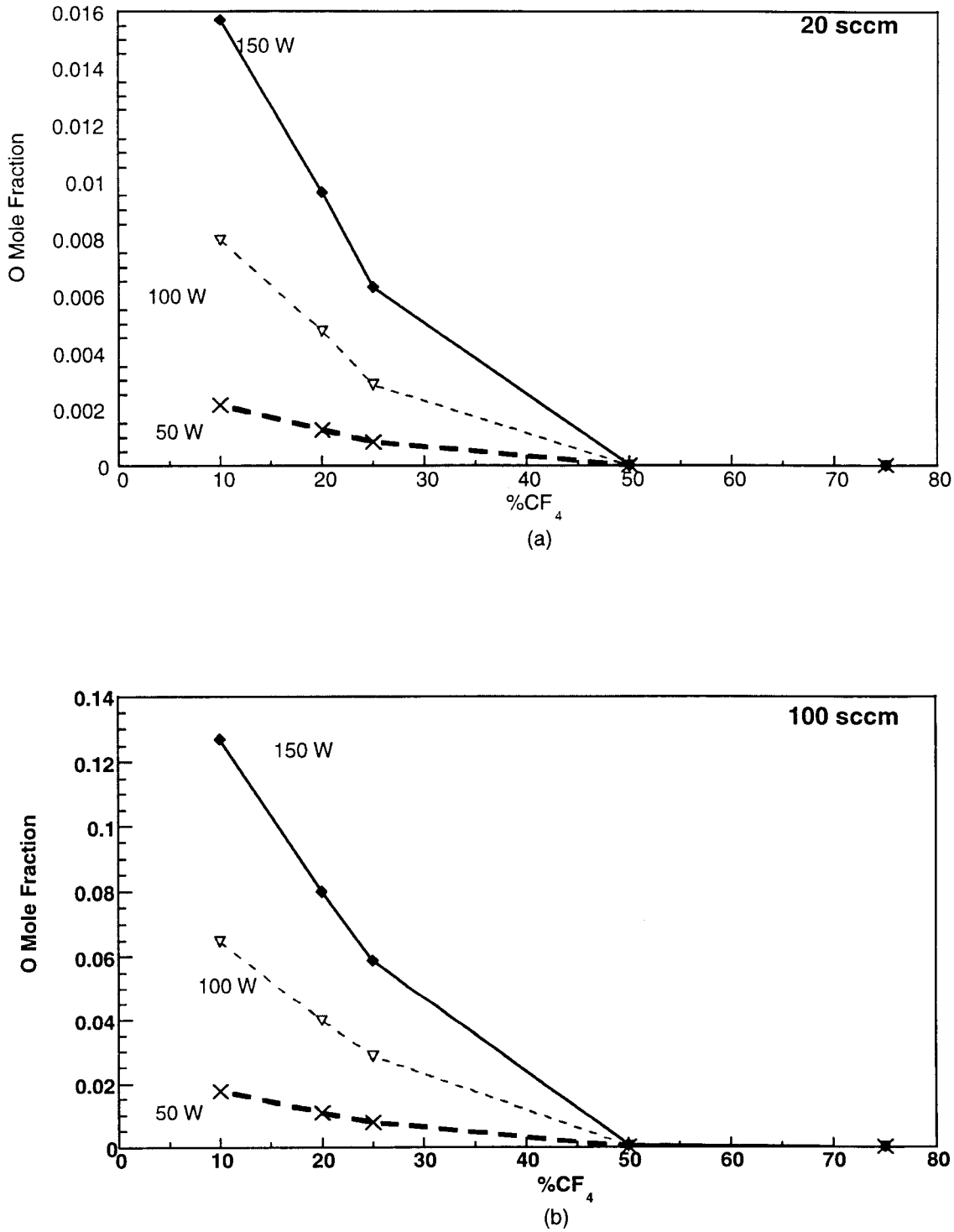

Figure 5.8: Mole Fraction of atomic oxygen as a function CF_4 concentration in the feed. Total pressure = 0.5 torr, flow rates = 20 and 100 sccm

The fraction conversion of CF_4 into the carbon containing stable products (CO_2, CO and COF_2) is defined as follows:

$$f_i = y_i / \left(y_{CF_4}\right)_{in}$$

where y_i is the mole fraction of species i at any distance x and $\left(y_{CF_4}\right)_{in}$ is the mole fraction of CF_4 in the feed gas mixture (x=0). Plotting f_i at the exit of the plasma region and 0.3 m downstream allows the effects of plasma reactions and homogeneous chemical reactions in the afterglow to be deconvoluted.

Figures 5.9 and 5.11 plot f_{CO_2}, f_{CO} and f_{COF_2} as a function of CF_4 conversion at 0.5 torr for two feed gas compositions. One composition is from the oxygen rich regime 20% CF_4/75% O_2/5%Ar, and one is from the fluorine rich regime, 75% CF_4/20% O_2/5% Ar, respectively. Similarly, Figures 5.10 and 5.12 plot the mole fraction of atomic oxygen, atomic fluorine and molecular fluorine as a function of CF_4 conversion for the same process conditions. A data set for each power (50, 100 and 150 W) contains simulated results obtained for flow rates of 20, 40, 60, 80 and 100 sccm. Therefore, each plot combines the results of all the flow rates at a given power. Data at the exit of the plasma and 0.30 m downstream of the plasma are labeled (a) and (b) respectively. The solid lines represent data collected at 50 W, the dotted at 100 W and the dashed lines at 150 W.

In Figure 5.9.a (plasma exit), the profiles of f_{CO_2}, f_{CO} and f_{COF_2} from one power to the next are nearly continuous. For conversions lower than 0.7, CO_2 is the major product. At higher conversions, CO becomes the dominant species. Furthermore, the

f_{CO_2} and f_{COF_2} profiles are parabolic and symmetric peaking at 0.5 while f_{CO} increases dramatically with conversions (f_{CO} varies from ~4.10^{-3} to 0.2). In Figure 5.9.b, which presents the data collected 0.3 m downstream of the plasma, the features of the f_i profiles are more intricate than those seen in Figure 5.9.a. CO_2 is always the major product and its concentration increases with conversion. The f_{COF_2} profile of remains similar to that at the plasma exit. In some cases, the species profiles are no longer continuous from one plasma power to the next (for example, f_{CO} at $x_{CF_4} = 0.7$).

Figure 5.10 plots the mole fraction of atomic oxygen, atomic fluorine and molecular fluorine as a function of CF_4 conversion at 0.5 torr for 20%CF_4/75% O_2/5% Ar. At the exit of the plasma (Figure 5.10.a), atomic fluorine is present at large concentrations while molecular fluorine is only present in minor concentrations (mole fraction less than 0.01). The concentrations of atomic fluorine and oxygen increase with CF_4 conversion and are nearly equal except at low CF_4 conversions. Downstream of the plasma (Figure 5.10.b), the profiles of atomic and molecular fluorine remain relatively similar to that observed at the plasma exit (Figure 5.10.a). However, the mole fraction of molecular fluorine is greater 0.3 m downstream of the discharge than it is at the plasma exit. Furthermore, the concentration profile of atomic oxygen changes significantly, decreasing at each power with increasing conversion. Hence, the concentration of atomic oxygen depends strongly on residence time, i.e., O is a reactant in the afterglow region.

Figure 5.11 plots f_{CO_2}, f_{CO} and f_{COF_2} as a function of CF_4 conversion at 0.5 torr for a 75% CF_4/20% O_2/5% Ar feed gas composition. In Figure 5.11.a (the plasma exit),

COF_2 is the major product and its concentration increases with conversion. The profiles of f_{CO_2} and f_{CO} follow the same trend as the one described in Figure 5.9.a where CO concentrations are lower than CO_2 concentration at conversions lower than ~0.4. Again, the species profiles are relatively continuous from one plasma power to the next. At 0.3 m downstream of the plasma (Figure 5.11.b), COF_2 remains the dominant carbon containing species. Its concentration profile does not change significantly from the one described in Figure 5.11.a. CO is the minor product and its concentration as well as that of CO_2 increase with conversion except at 150 W.

Figure 5.12 plots the mole fraction of the reactive atomic oxygen, atomic fluorine and molecular fluorine as a function of conversion for 75%CF_4/20% O_2/5% Ar at 0.5 torr. In Figure 5.12.a (plasma exit), atomic fluorine is the dominant species; the F concentration profile as well as that of atomic oxygen increase with CF_4 conversion.; however, at the plasma exit, oxygen atoms are present is small concentrations (mole fraction less than 10^{-4}). Again, molecular fluorine is always small with mole fractions less than 0.01. In Figure 5.12.b, the profiles of atomic and molecular fluorine remain similar to that observed at the exit of the plasma. However, the O atom mole fraction approaches zero. Virtually, all the oxygen atoms react by the time they are transported down the tube.

In the plasma region, both electron impact dissociation and homogeneous reactions occur. The majority of the carbon containing species produced by gas phase reactions, also participate in electron impact dissociation reactions. The balance between the formation and the loss of those species creates the continuous features of the

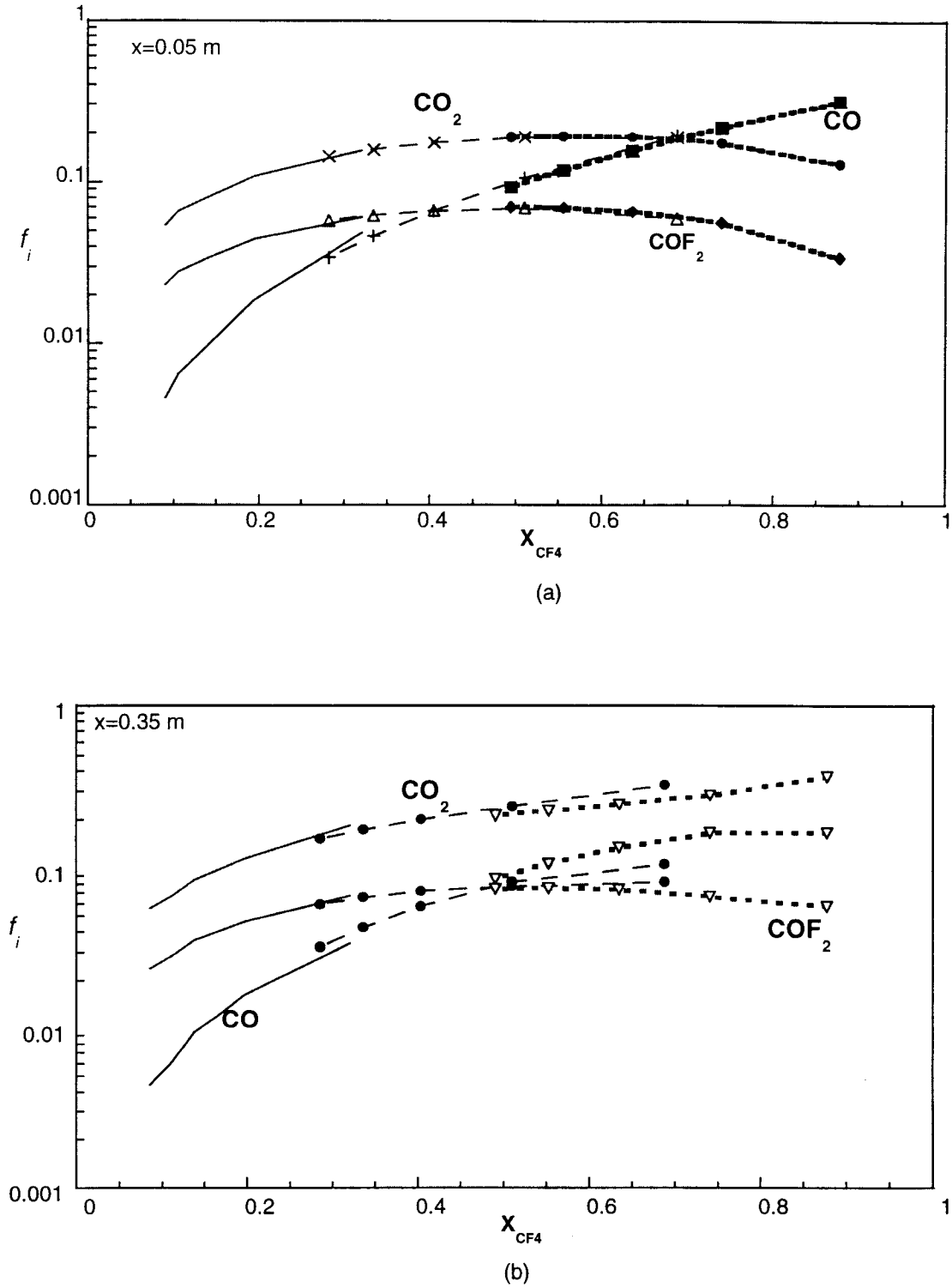

Figure 5.9: f_{CO_2}, f_{CO} and f_{COF_2} as a function of CF_4 Conversion for 20%CF_4/75%O_2/5% Ar. Total Pressure = 0.5 torr, flow rate = 20, 40, 60, 80 and 100 sccm. The solid lines represent data collected at 50 W, the dotted at 100 W and the dashed lines at 150 W.

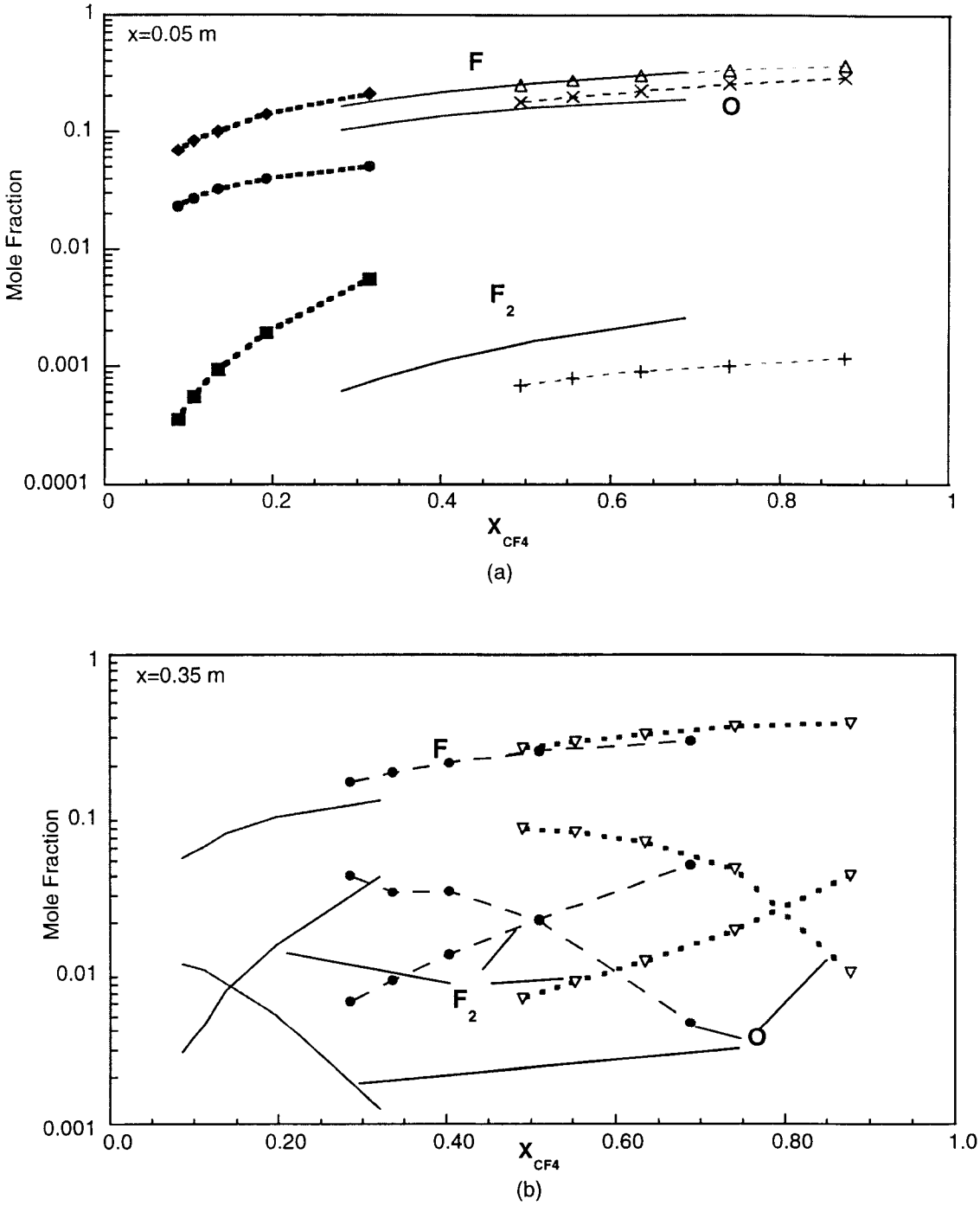

Figure 5.10: Mole Fraction of O, F and F_2 for 20%CF_4/75%O_2/5% Ar. Total Pressure = 0.5 torr, flow rate = 20, 40, 60, 80 and 100 sccm. The solid lines represent data collected at 50 W, the dotted at 100 W and the dashed lines at 150 W.

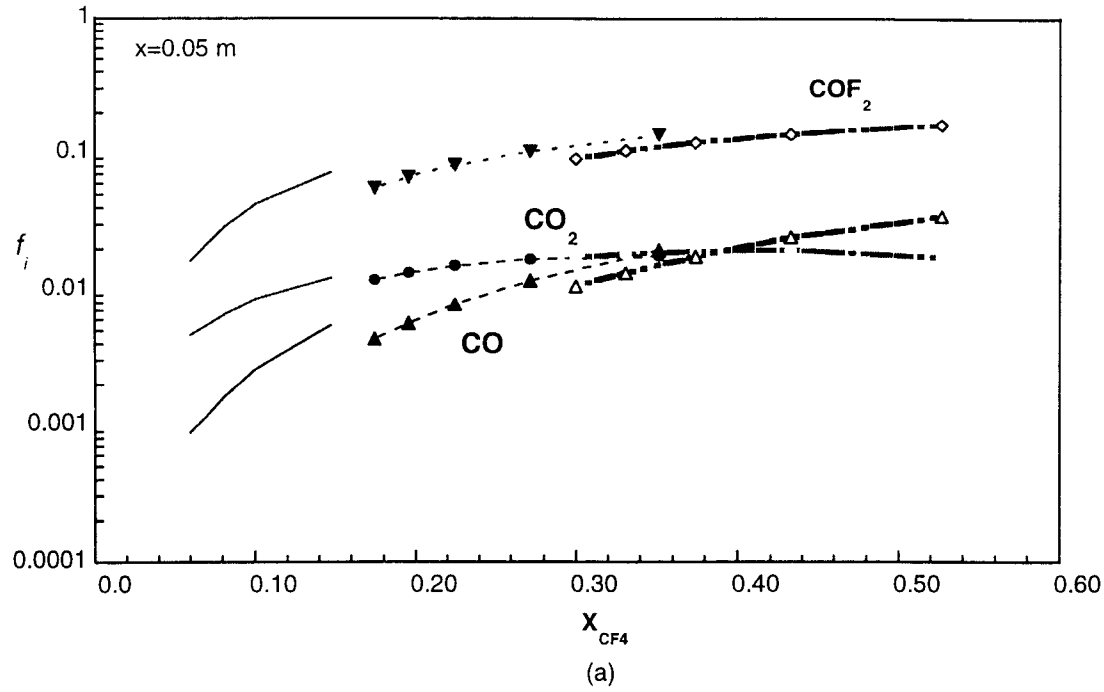

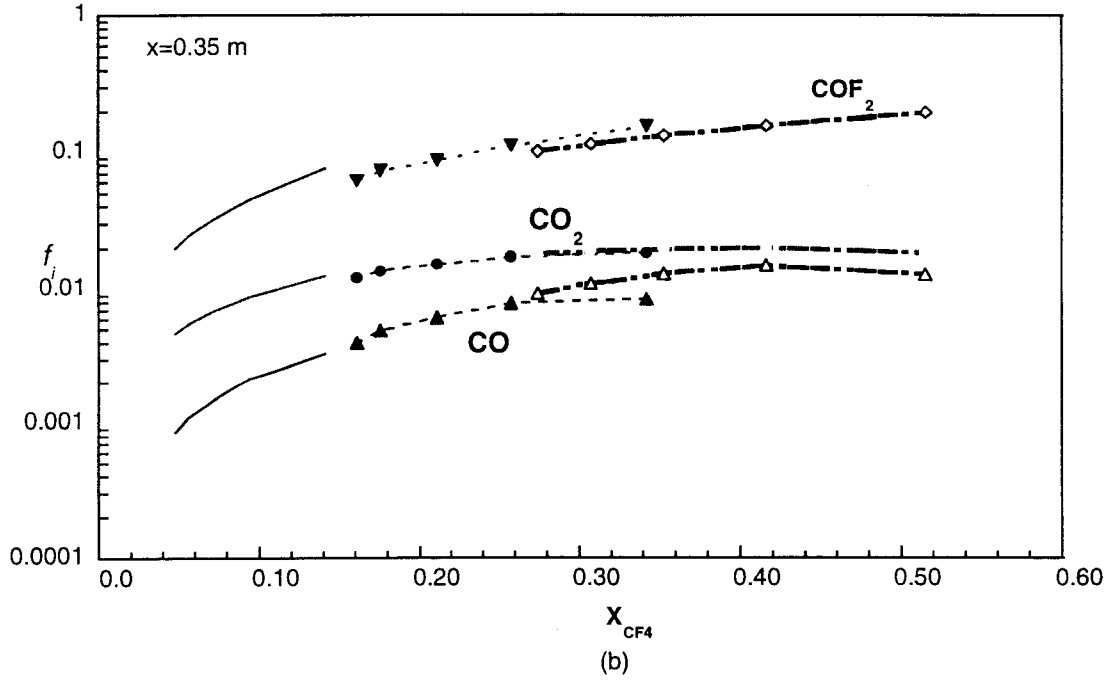

Figure 5.11: f_{CO_2}, f_{CO} and f_{COF_2} as a function of CF_4 Conversion for 75%CF_4/20%O_2/5% Ar. Total Pressure = 0.5 torr, flow rate = 20, 40, 60, 80 and 100 sccm.. The solid lines represent data collected at 50 W, the dotted at 100 W and the dashed lines at 150 W.

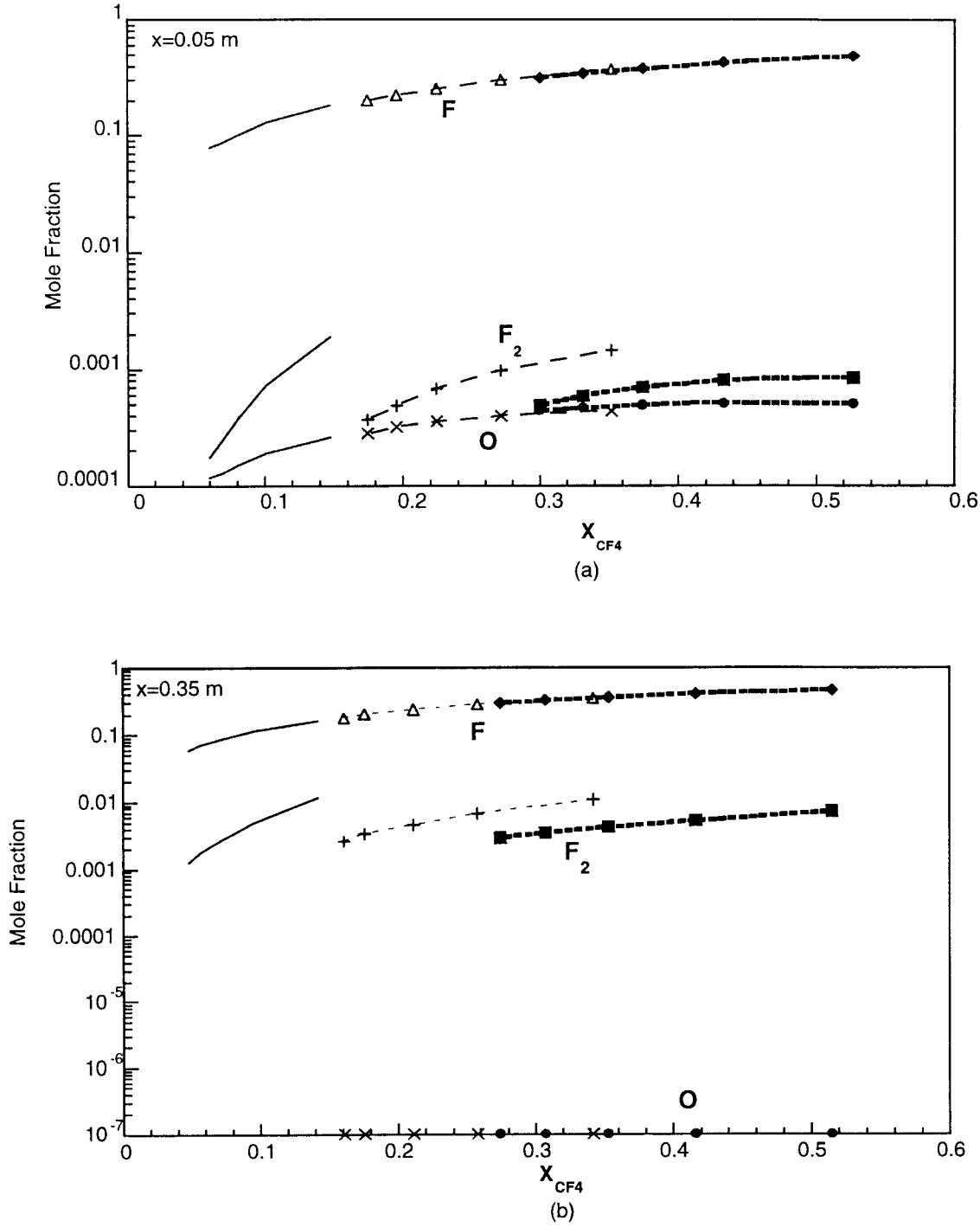

Figure 5.12: Mole Fraction of O, F and F_2 for 75%CF_4/20%O_2/5% Ar. Total Pressure = 0.5 torr, flow rate = 20, 40, 60, 80 and 100 sccm. The solid lines represent data collected at 50 W, the dotted at 100 W and the dashed lines at 150 W.

concentration profiles seen in Figure 5.9.a. As electron impact reactions cease in the afterglow region, some of the concentration profiles seen the exit of the afterglow region (Figure 5.9.b) are no longer continuous.

Figure 5.13 shows a summary of the major reaction pathways in the oxygen rich regime (heavy solid arrows). Dashed arrows indicate the minor reaction pathways.

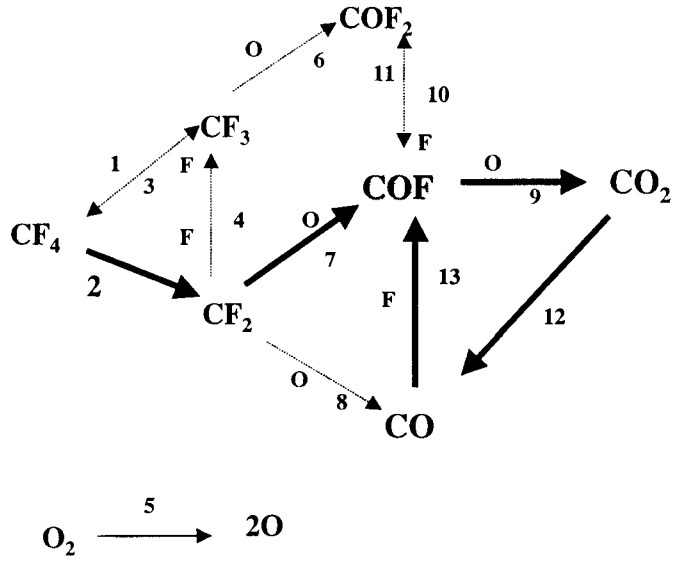

Figure 5.13: Major reaction pathways in the oxygen rich regime

At the plasma exit, CO is the major product at high conversions while the CO concentration is always lower than the CO_2 concentration at the exit of the afterglow region. Therefore, the electron impact dissociation of CO_2 is a major source of CO production in the system. In the afterglow, CO recombines with O, as shown by reaction

9 and 13, to form CO_2. The effect of this reaction is further illustrated by changes in the concentration profiles of O between the plasma exit (Figure 5.10.a) and the exit of the afterglow (Figure 5.10.b).

Because of recombination reactions (gas phase or surface wall recombination), O atom concentration decreases with increasing residence time in the afterglow region and the concentration profile is seen as residence time dependent in Figure 5.10.b.

In the afterglow, fluorine atoms are both created (reaction 9) and lost (reaction 13) by homogeneous reactions. Consequently, the balance between the creation and loss of atomic fluorine is seen in the relatively unaltered F concentration profiles in the afterglow. The recombination reactions involving atomic fluorine produce molecular fluorine or COF (reaction 13) which is ultimately converted to either CO_2 (predominantly in the O rich regime) or COF_2 (predominantly in the CF_4 rich regime). The similarities between the concentration profiles in Figures 5.9.a and 5.9.b further indicate the following:

- The direct reaction of CF_3 and atomic oxygen (reaction 6) is a minor pathway for COF_2 production in the system. The minor effect of reaction 6 is to be expected since the concentration of CF_3 radicals is low because of the selected CF_4 dissociation branching ratio.
- In the oxygen rich regime, COF reacts more favorably with O atoms to form CO_2 and CO and reaction 10 has little effect on the product distribution.

The major reactions pathways in the CF_4 rich regime are shown in Figure 5.14 (solid arrows). Dashed arrows represent the minor reactions.

Because of recombination reactions (gas phase or surface wall recombination), O atom concentration decreases with increasing residence time in the afterglow region and the concentration profile is seen as residence time dependent in Figure 5.10.b.

In the afterglow, fluorine atoms are both created (reaction 9) and lost (reaction 13) by homogeneous reactions. Consequently, the balance between the creation and loss of atomic fluorine is seen in the relatively unaltered F concentration profiles in the afterglow. The recombination reactions involving atomic fluorine produce molecular fluorine or COF (reaction 13) which is ultimately converted to either CO_2 (predominantly in the O rich regime) or COF_2 (predominantly in the CF_4 rich regime). The similarities between the concentration profiles in Figures 5.9.a and 5.9.b further indicate the following:

- The direct reaction of CF_3 and atomic oxygen (reaction 6) is a minor pathway for COF_2 production in the system. The minor effect of reaction 6 is to be expected since the concentration of CF_3 radicals is low because of the selected CF_4 dissociation branching ratio.
- In the oxygen rich regime, COF reacts more favorably with O atoms to form CO_2 and CO and reaction 10 has little effect on the product distribution.

The major reactions pathways in the CF_4 rich regime are shown in Figure 5.14 (solid arrows). Dashed arrows represent the minor reactions.

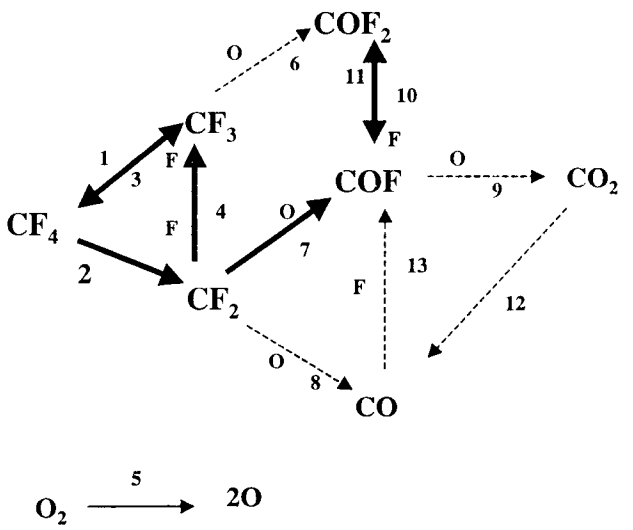

Figure 5.14: Major reaction pathways in the CF_4 rich regime.

Again, the electron impact dissociation of CO_2 in the plasma is seen as the major pathway of CO formation in the CF_4/O_2 discharge plasma. But contrary to observations made in the oxygen rich regime, the CO_2 concentration profile is relatively the same in both Figures 5.11.a and 5.11.b at with flat slopes at 150 W. These similarities denote an apparent CO_2 production saturation, which is more pronounced at high CF_4 conversions. Therefore, reaction 9 is negligible in the afterglow and the recombination reaction between CO and F (reaction 13) accounts for the drop in CO concentration seen in Figure 5.12.b. However, the concentration profiles of both COF_2 and F remain relatively the same in Figures 5.11 and 5.12. This further indicates that:

- The above reaction pathway (reaction 13) is minor in the afterglow region.
- Reaction 3 (CF_3 +F recombination) which severely limits CF_4 conversion in this regime, is the major reaction pathway in the CF_4 rich regime.

Furthermore, surface wall recombination accounts primarily for the loss of atomic oxygen in the afterglow region.

5.5 Effects of Pressure

Figure 5.15 plots CF_4 conversion as a function of residence time for a 20% CF_4/75%O_2/5%Ar feed gas mixture. Two pressures studied, 0.2 and 0.8 torr, are labeled (a) and (b), respectively. The results are presented for the distance 0.3 m downstream the plasma at the exit of the afterglow region. The flow rate is varied from 20 to 100 sccm.

As observed earlier in Figure 5.3 for simulations performed at 0.5 torr, CF_4 conversion is, in most cases, proportional to power and increases with residence time. At 50 W, the conversion increases linearly with residence time. For a given flow rate and power, CF_4 conversion increases as pressure decreases. This decrease is to be expected since the average electron energy in the plasma, therefore the EEDF, decreases with pressure. Since most inelastic collisions require high energies, lowering the pressure results in higher electron dissociation rate constants.

Figure 5.16 plots the mole fraction of the carbon containing species (CO_2, CO and COF_2) as a function of CF_4 conversion for a 20% CF_4/75%O_2/5% Ar feed gas mixture and simulations results obtained 0.3 m downstream the plasma. At 0.2 torr (Figure 5.16.a), again at conversions lower than 0.7, CO_2 is the major product while CO becomes the dominant species at higher conversions. CO mole fraction increases dramatically with CF_4 conversion from 0.02 (50 W and 100 sccm) to 0.15 (150 W and 20 sccm). The species concentration profiles are continuous from one power to the next except at 150

W. Above 0.5, the COF_2 concentration profile decreases parabolicly. In Figure 5.16.b (0.8 torr), CO_2 is the major product. The CO_2 concentration increases with conversion. At 100 and 150 W, CO_2 increases linearly with CF_4 conversion. COF_2 is the minor product; the COF_2 concentration increases sharply with CF_4 conversion at 50 and 100 W. At 150 W, there is an apparent saturation in CO and COF_2 production, the concentrations are nearly equal and the profiles shows little variation.

Although the data presented in Figure 5.16.a is collected 0.3 m downstream the plasma cavity, the major trends are similar to the ones seen in Figure 5.9.a (for simulation results obtained at the plasma exit and 0.5 torr). The observation strongly suggests that, at low pressures, the species distribution and concentration are mainly dominated by electron impact dissociation reactions. At high conversion, a major fraction of the CO_2 formed is dissociated into CO and the homogeneous recombination reactions in the afterglow are apparently limited by the surface wall recombination of atomic oxygen. At this lower pressure, homogeneous reactions are less important. Conversely, at 0.8 torr, the chemistry is dominated by recombination reactions which is seen in the increase of CO_2 concentration with CF_4 conversion. Only a small fraction of CO_2 is dissociated by electrons in the plasma; therefore at higher pressures, the effects of recombination in the afterglow region are more important.

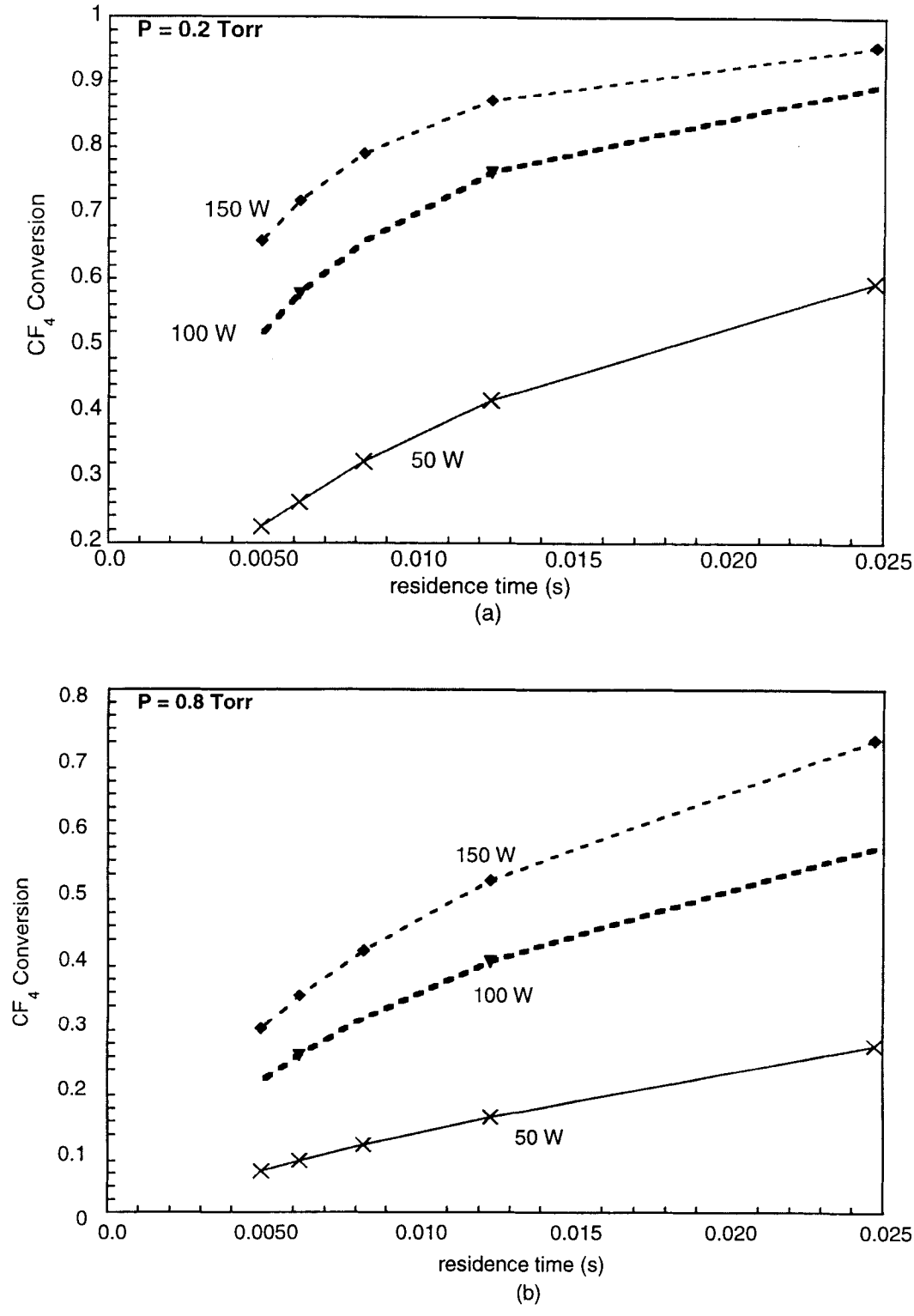

Figure 5.15: CF_4 Conversion as a function of residence time for a 20%CF_4/75% O_2/5%Ar gas mixture. Total Pressure = 0.2 and 0.8 torr, Plasma power = 50, 100, 150 W. Simulation results 0.3 m downstream of plasma exit.

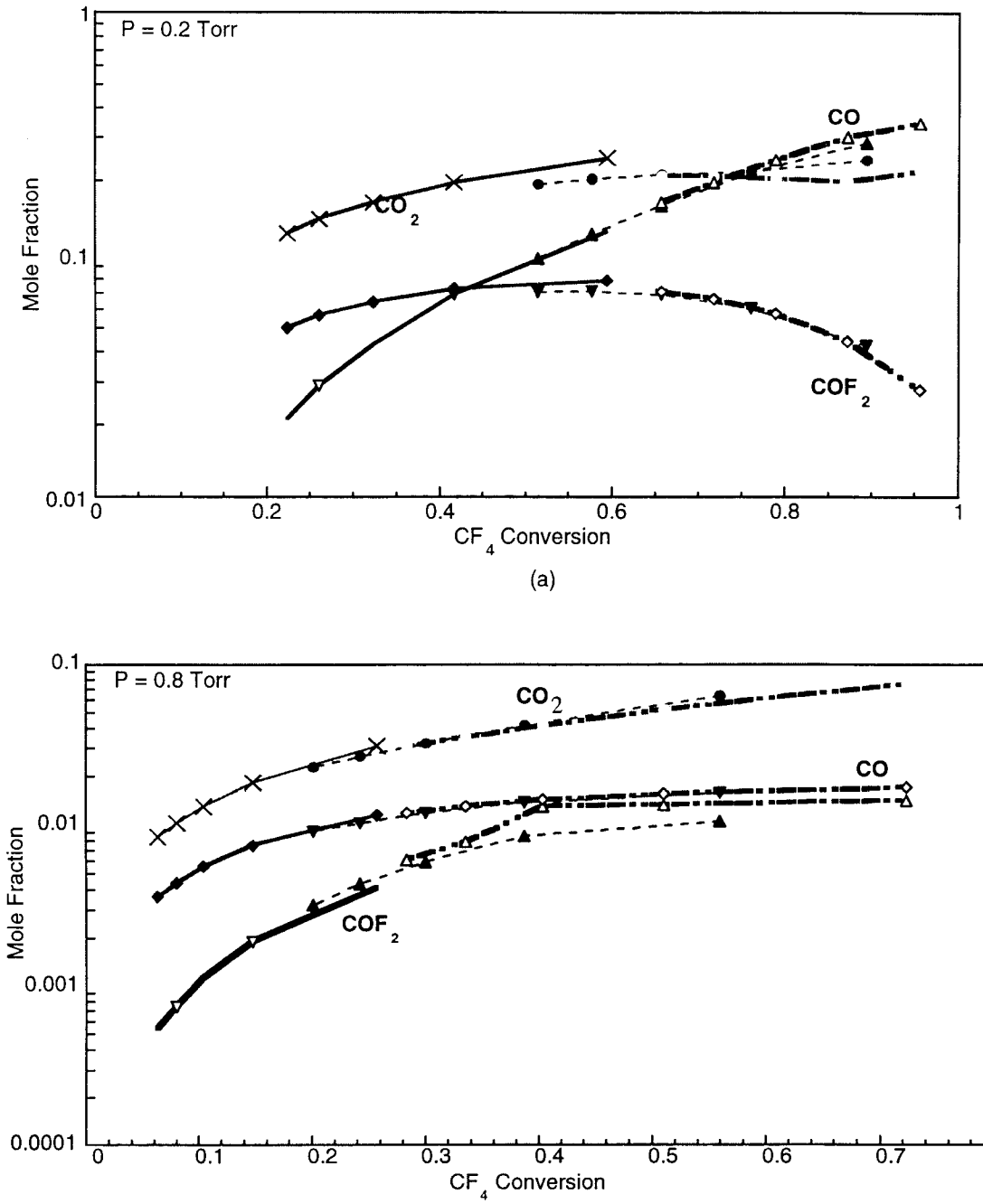

Figure 5.16: Mole Fraction of CO_2, CO and COF_2 as a function of CF_4 conversion for a 20%CF_4/75% O_2/5%Ar gas mixture. Total Pressure = 0.2 and 0.8 torr, Plasma power = 50, 100, 150 W. Simulation results 0.3 m downstream of plasma exit. The solid lines represent data collected at 50 W, the dotted at 100 W and the dashed lines at 150 W.

CHAPTER 6

CONCLUSIONS AND RECOMMENDATIONS

6.1 Conclusion

The gas phase chemistry of a CF_4/O_2 microwave plasma and afterglow region of our laboratory was studied. The rate coefficient of the electron impact dissociation reactions were determined using both literature collision cross section data and plug flow analysis of data collected in our laboratory. Fluid simulations of the model were performed using computational fluid dynamics and the simulated results were compared to mass spectrometer experimental data. The good agreement between model predictions and experimental data encouraged further simulations to investigate the effects of plasma power, feed composition, residence time and pressure on the chemistry of the system. The results of this study may be summarized as follow:

1. Both homogeneous recombination reactions and plasma-induced reactions affect the chemistry of the CF_4/O_2 microwave plasma.
2. CF_4 conversion increases with plasma power and residence time.
3. The product distribution falls into two regimes: the oxygen rich regime and the CF_4 rich regime.
4. In the oxygen rich regime (below 25 mole % CF_4 in the feed), CO_2 and CO are the major products of CF_4 decomposition. The homogeneous recombination reactions in the afterglow region are controlled by reactions of the free radicals and intermediate species with atomic oxygen. These reactions limit CF_3 and

atomic fluorine recombination to form CF_4 leading to high CF_4 conversions.

5. In the CF_4 rich regime (above 50 mole % in the feed), COF_2 is the major product. In the afterglow region, the recombination of CF_3 with F to reform CF_3 becomes the controlling mechanism and severely limits CF_4 conversion.
6. Changes in pressure affect adversely CF_4 conversion. The conversion increases with decreasing pressure and decreases with increasing pressure. At lower pressures, the gas phase chemistry mechanism is controlled by the electrons impact dissociation reactions. At higher pressures, lower conversions are achieved and the effects of recombination reactions are more important in the afterglow region.

6.2 Recommendations for Future Work

The kinetic model developed reproduces qualitatively the general trends of the experimental data. In order to improve the quantitative agreement between the model and the experimental data, some recommendations are given below:

- Modify the quantification of the branching ratio of CF_4 electron impact dissociation into CF_3 and CF_2.
- Use the rate coefficient of CF_3 and F recombination to form CF_4 as a fitting parameter in the model.

The model provided a better understanding of the chemistry of the CF_4/O_2 plasma. Future works can be aimed at developing a similar model for more complicated and less studied plasma systems such as the NF_3/O_2 discharge plasma.

BIBLIOGRAPHY

1. Baltes, H. P., Schoenborn, P. and Roger, P., "Numerical simulation of a CF_4/O_2 plasma and correlation with spectroscopic and etch rate data," J. Electrochem. Soc., 136, 199 (1989).

2. Bell, A. T., Hollahan, J. R., "Techniques and applications of plasma chemistry," Wiley, New York (1974).

3. Bonham, R.A. and Bruce M.R., Intern. J. Mass Spectrom. Ion Processes, 123, 97 (1993).

4. Chou, C., Wei, T. and Phillips, J., " Detail model of the afterglow region of a microwave generated oxygen plasma," J. Appl. Phys., 72, 870 (1992).

5. Christophorou, L. G., Olthoff, J. K., and Rao M. V. V. S., "Electron interactions with CF_4," J. Phys. Chem. Ref. Data, 25, 1341 (1996).

6. Davies, H. L. and M.Y. Smith in Proceedings of the Eighth Australian Computer Conference, Australian Computer Soc. Inc, 1, 277 (1978).

7. Economou, D. J., and Park S., "A mathematical model for a plasma-assisted downstream etching reactor," J. Appl. Phys., 66, 3256 (1989).

8. Hsu, K., "Smear removal and microvia drilling of printed circuits boards by microwave plasma processes," Ph.D research proposal (1997).

9. Itikawa, Y. and Ichimura, A., "Cross sections for collisions of electrons and photons with atomic oxygen," J. Phys. Chem. Ref. Data, 19, 637 (1990).

10. Itikawa, Y., Ichimura, K., Onda, K., Sakimoto, K., Takayanagi, K., Hatano, K., Hayashi, M., Nishimura, H. and Tsurubuchi, S., "J. Phys. Chem. Ref. Data, 18, 23 (1989).

11. Jensen, K. F. and Dalvie, M., "Combined experimental and modeling study of spatial effects in plasma etching," J. Electrochem. Soc., 137, 1062 (1990).

12. Mantzaris, N. V, Boudouvis. A. and Gogolides, E., " Radio-frequency Plasma in CF_4: self-consistent modeling of the plasma physics and chemistry," J. Appl. Phys, 12, 6169 (1995).

13. Moisan, M., Sauve, G., Paraszczack, J. R. and Heidenreich, J. E., "Electron energy distributions in oxygen microwave plasmas," J. Vac. Sc. Technol. B, 6, 288 (1988).

14. Myers, H., "Analysis of electron swarm experiments in oxygen," J. Phys. B. (Atom. Molec. Phys.), 2, 393 (1969).

15. Plumb, I. C. and Ryan, K. R., "A model of the chemical processes occuring in CF_4/O_2 discharges used in plasma etching," Plasma Chem. Plasma Process., 6, 231 (1986).

16. Plumb, I. C. and Ryan K. R., "Gas-phase reactions of CF_2 with $O(^3P)$ to produce COF: their significance in plasma processing," Plasma Chem. Plasma Process., 4, 271 (1984).

17. Plumb, I. C. and Ryan K. R., "Gas phase reactions of CF_3 and CF_2 with atomic and molecular fluorine: their significance in plasma etching," Plasma Chem. Plasma Process., 6, 11 (1986).

18. Smolinsky, G. and Flamm, D. L., "The plasma oxidation of CF_4 in a tubular-alumina fast flow reactor," J. Appl. Phys., 50, 4982 (1979).

19. Sugai H., Toyoda H., Nakano T., and Goto M., "Absolute cross sections for the electron impact dissociation of CF_4 and CHF_3 into the CF_x (x = 1 - 3) neutral radicals," Contrib. Plasma Physics., 35, 415 (1995).

20. Tarvnovsky, V., Kurunczi, P., Rogozhnikov, D. and Becker, K., "Absolute cross sections for the dissociative electron impact ionization of the CF_x (x = 1 - 3) free radicals," Int. J. Mass Spectrom. Ion Processes, 128, 181 (1993).

21. Venkatesan, S. P., Trachtenberg, I. and Edgar, T. F., " Modeling of silicon etching in CF_4/O_2 and CF_4/H_2 plasmas," J. Electrochem. Soc., 137 (1990).

22. Winters, H. F and Inokuti, M., "Total cross section of CF_4 and other fluoroalkanes for electron impact," J. Phys. Rev. A, 25, 1420 (1982).

APPENDIX

Figures A1 and A2 represent velocity profiles resulting from fluid simulations of the more complicated geometry which includes both the alumina tube and the substrate. The contour plots are obtained from Fluent and done for two volumetric flow rates: 20 and 100 sccm.

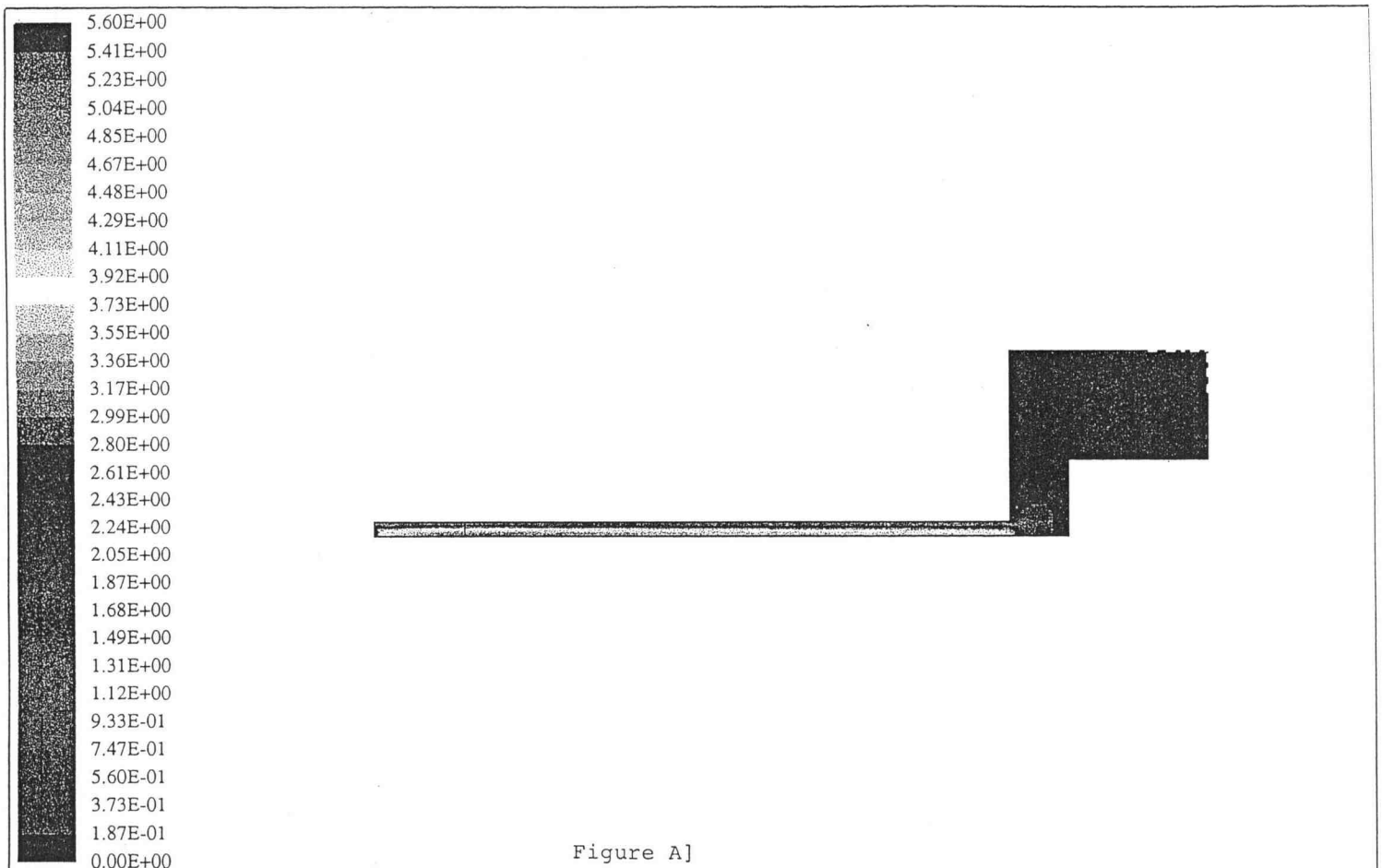

Figure A]

VELOCITY PROFILE FOR Q=20 SCCM
Velocity Magnitude (M/S)
Max = 5.600E+00 Min = 0.000E+00

Aug 01 1997
Fluent 4.42
Fluent Inc.

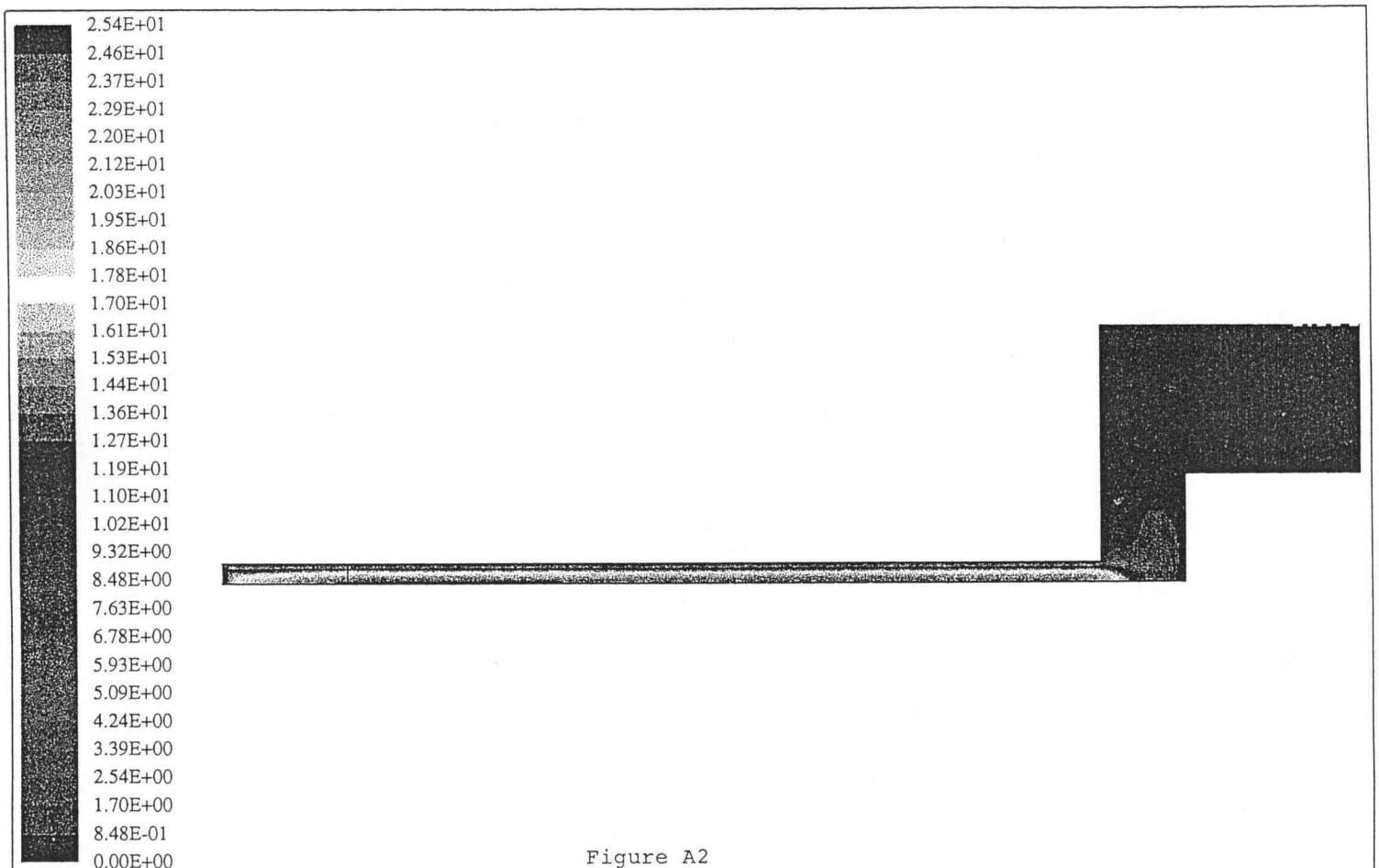

Figure A2

Y Z X	VELOCITY PROFILE ALONG REACTOR FOR Q=100 SCCM Velocity Magnitude (M/S) Max = 2.543E+01 Min = 0.000E+00	Aug 01 1997 Fluent 4.44 Fluent Inc.